Measurements of local electric fields by Doppler-free laser spectroscopy of hydrogen resonance lines

DISSERTATION

zur Erlangung des akademischen Grades
doctor rerum naturalium
(Dr. rer. nat.)
im Fach Physik

eingereicht an der
Mathematisch-Naturwissenschaftlichen Fakultät I
Humboldt-Universität zu Berlin

von
M.Sc.-Phys. (Univ. Belgrad, Jugoslawien) Minja Gemišić Adamov
geboren am 23.03.1974 in Bor

Präsident der Humboldt-Universität zu Berlin:
Prof. Dr. Christoph Markschies

Dekan der Mathematisch-Naturwissenschaftlichen Fakultät I:
Prof. Thomas Buckhout, Ph.D.

Gutachter:

1. Prof. Dr. Gerd Fußmann
2. Priv.-Doz. Dr. Joachim Seidel
3. Prof. Dr. Oliver Benson

eingereicht am: 19. Mai 2006
Tag der mündlichen Prüfung: 15. August 2006

Abstract

A method for electric field measurements that observes the Stark spectra of the low excited levels $n = 2$ and $n = 3$ of atomic hydrogen has been explored in this work. As advantage these levels can be excited Doppler-free from the ground state by a single laser and the highly resolved Stark spectra are easy to understand and to be calculated. Good sensitivity of electric field measurements is achieved with specially designed solid state laser systems, which provide tuneable pulsed UV radiation with a high pulse peak-power and a narrow bandwidth needed for Doppler-free two-photon excitation. Using hydrogen and deuterium the Stark spectra of the $n = 2$ level are detected as optogalvanic signal. For three different cases of laser polarization the $n = 3$ spectra of hydrogen are measured simultaneously with optogalvanic and laser induced Balmer alpha fluorescence detection. Electric fields down to 200 V/cm can be determined from the Stark spectra of $n = 2$ level, while the spectra of $n = 3$ level enable measurements of electric fields as small as 50 V/cm in each of the three cases of laser polarization.

Keywords:
hydrogen atom, electric field, laser spectroscopy, UV-laser systems

Zusammenfassung

In dieser Arbeit wurde eine einfache laserspektroskopische Messmethode für lokale elektrische Feldstärken im Hinblick auf ihre Messmöglichkeiten und -grenzen untersucht. Als empfindliche optische Feldsensoren dienen dabei Wasserstoffatome, für die die Stark-Aufspaltung der Spektrallinien im elektrischen Feld wohl bekannt und exakt berechenbar ist. Zudem sind Wasserstoffatome sowieso in vielen Gasentladungen und technologisch bedeutsamen Plasmen vorhanden, und die genaue Kenntnis der elektrischen Feldstärkeverteilung ist eine wesentliche Voraussetzung für das Verständnis der Plasmaerzeugung und die Prozessoptimierung.

Die experimentellen Untersuchungen wurden an einer Niederdruck-Gaszelle durchgeführt, in der ein elektrisch geheizter Wolframdraht für thermische Dissoziation von Wasserstoffmolekülen sorgte. Eine einstellbare Spannung zwischen diesem und einem parallel angeordneten benachbarten Draht erzeugte das elektrische Feld. In der Mitte zwischen den Drähten wurden die Wasserstoffatome durch zwei gegenläufige Laserstrahlen Doppler-frei angeregt. Die Durchstimmung der schmalbandigen Laserstrahlung über den Wellenlängenbereich der Zwei-Photonen-Resonanz lieferte direkt das vom elektrischen Feld hervorgerufene Stark-Spektrum des angeregten Zustands.

Weil die Methode im Gegensatz zu ähnlichen, erheblich aufwendigeren Verfahren nur die niedrigsten Wasserstoff-Energieniveaus benutzt, die mit Zwei-Photonen-Anregung direkt aus dem Grundzustand erreichbar sind, kommt sie mit einem einzigen Laser aus. Für das erste angeregte Niveau mit $n = 2$ wird Strahlung bei 243 nm benötigt, das nächsthöhere Niveau mit $n = 3$ erfordert 205 nm. Für beide Wellenlängen konnte mit je einem abstimmbaren, gepulsten Einmoden-Lasersystem die erforderliche hohe spektrale Auflösung erreicht werden, nachdem das 205-nm-System zunächst im Rahmen dieser Arbeit verbessert worden war.

Für $n = 2$ wurden Untersuchungen an Wasserstoff und Deuterium durchgeführt und Stark-Spektren mittels optogalvanischer Detektion gemessen. Schwerpunkt der Arbeit waren aber die Messungen an Wasserstoff für $n = 3$, bei denen zusätzlich Balmer-alpha-Fluoreszenz im Sichtbaren zur Detektion eingesetzt werden konnte. Bei elektrischen Feldern bis 200 V/cm wurden Stark-Spektren für drei verschiedene Polarisationszustände der Laserstrahlung aufgenommen. Als Ergebnis konnte jeweils ein Paar isolierter Stark-Komponenten in den Spektren identifiziert werden, dessen gut messbarer Frequenzabstand durch Vergleich mit theoretischen Werten die Bestimmung der elektrischen Feldstärke ermöglicht. Die verwendeten optimierten Lasersysteme erlaubten die Bestimmung kleiner elektrischer Feldstärken mit einer Messunsicherheit von etwa 10 V/cm, einer Zeitauflösung im Nanosekundenbereich und einer räumlichen Auflösung, die nur durch das Fluoreszenz-Nachweissystem begrenzt war.

Schlagwörter:
Wasserstoffatom, elektrisches Feld, Laserspektroskopie, UV-Lasersysteme

Contents

List of Figures

List of Tables

Chapter 1

Introduction

The electric field is one of the most important parameters of gas discharges and its determination has always been one of the challenges for discharge diagnostics. The knowledge of electric field distributions helps in understanding and controlling the discharge processes and gives useful information for discharge modeling or the determination of other plasma parameters that are closely connected to the electric field. Some of the parameters that can be deduced from electric field values are densities, fluxes and energy distributions of charged particles [2, 3]. Characterization of the cathode fall and negative glow regions of glow discharges requires electric field mapping which is also important for other low pressure plasmas such as radio frequency driven discharges, plasma switches or edge regions of high temperature fusion plasmas. Optimization of technological low temperature plasmas, which are widely applied e.g. for plasma etching of semiconductors or various plasma deposition processes, requires information about the magnitude and the distribution of the electric field in the plasma volume near the surface of interest.

According to the need for electric field determination in plasma diagnostics, various methods have been developed. The methods using different types of electrostatic probes are inevitably perturbing the measured plasma [4]. Also electron beam deflection is perturbing and limited to low pressure and low current density plasmas [5]. The influence of the electric field on the structure of emitted spectral lines has been known as the Stark effect [6] since long and presents the basis of the optical measurements of electric fields. To the best advantage, optical emission spectroscopy is completely non-intrusive. However the electric field sensitivity is limited by other line-broadening mechanisms, in particular the Doppler broadening. Those limitations can be partly overcome by calculating or measuring the other effects and taking them into account in the analysis of the measured Stark spectra [7, 8, 9].

Among the non-perturbing techniques developed for electric field measurements in plasmas, laser spectroscopic methods benefit from the laser development in the last twenty years and provide superior spatial and temporal resolution [10]. As field sensitive spectator particles whose Stark spectra are used for electric field measurement, various atomic species are utilized, especially H, He and Ar or hetero-nuclear diatomic molecules, because their Stark spectra are particularly suited for this kind of measurement. The hydrogen atom holds a special position because it plays also a key role for many plasma processes in technical applications as well as in fusion research. The Stark splitting of its highly field sensitive excited levels has been known for a long time [11]. A comprehensive description of these laser spectroscopic methods is given in Chapter 3.

In the frame of this work, a simple sensitive optical method for electric field measurement is explored in detail with respect to its possibilities and limitations. This method uses a single laser for the Doppler-free two-photon excitation of the low excited levels of hydrogen atoms, namely $n = 2$ or $n = 3$, and direct observation of the Stark splitting of these levels.

As the Stark effect of the excited levels in atomic hydrogen scales with the square of the principle quantum number n, higher levels are more sensitive to an external electric field. Therefore the observation of higher excited (Rydberg) levels is desirable. On the other hand, excitation of higher levels is experimentally more demanding. Starting with atoms in the ground state, two-photon laser excitation gives direct access only to $n = 2$ and $n = 3$. Higher levels would require a laser wavelength below 200 nm. At those wavelengths in the vacuum ultraviolet spectral range, tunable laser radiation can not be achieved with good performances. That is the reason why higher levels are excited via $n = 2$ or $n = 3$ with an additional second laser [12, 13]. This significantly increases the complexity of the experimental set-up. At the same time the spectra of the excited levels are more compound, individual Stark-components are hardly resolved and a comparison of the whole spectra with theoretical results is necessary to obtain an electric field value. In our one-step excitation method, which observes the simple Stark spectra of the low excited levels of atomic hydrogen, a good field sensitivity is achieved as result of the high performance of the laser system employed.

The measurements are performed in a special low pressure hydrogen cell where atomic hydrogen is produced by thermal dissociation. A variable electric field is established between the filament heated for dissociation and another grounded wire set parallel to it. The hydrogen atoms are excited from the ground state with two counter-propagating laser beams of the same wavelength. This provides spectra without Doppler broadening and gives the possibility for direct Stark splitting measurements. The narrow bandwidth of the tunable pulsed laser systems developed in our group enables the required high spectral resolution. One solid state laser optimized to provide radiation tunable at 243 nm is employed for two-photon excitation of the 1s-2s transition, and the second system is improved to produce stable pulsed radiation precisely tunable at 205 nm for the 1s-3s/d transition. The Stark spectra of the $n = 2$ levels of hydrogen and deuterium are observed as optogalvanic signals, while optogalvanic detection and laser induced Balmer alpha fluorescence detection are simultaneously utilized for the $n = 3$ level of hydrogen. The latter method is of main interest in this work, because the $n = 3$ level is more sensitive to the external electric field and provides the possibility of fluorescence detection in the visible part of the spectrum. Since optogalvanic detection cannot be applied in all plasma sources, fluorescence detection is preferable in general.

The use of the Stark splitting of the $n = 3$ level of hydrogen in combination with Balmer alpha fluorescence detection was originally proposed by Booth et al. in 1996 [14]. They performed only a measurement with two photons linearly polarized parallel to the external electric field, but from theoretical calculations they expected a better field sensitivity with photons linearly polarized perpendicular to the electric field. Here, both of these cases of laser polarization are investigated in detail, and an additional case with circularly polarized laser beams exciting only $\Delta m = 0$ transitions is investigated as well. Only with circular polarization the signal is independent of the direction of the electric field, which is advantageous in cases where the direction is not known. For each of the three cases the aim is to find a suitable field sensitive parameter of the Stark spectrum which can be easily compared with calculated values and thus can be used for electric field determination. A field-dependent frequency shift between two line components in the spectrum is preferred as parameter because measured signal sizes of line components are influenced by many different factors.

This thesis is organized in the following way. Chapter 2 reviews the theoretical basis important for understanding the physical background of this work. The structure of the hydrogen atom, its Stark effect, two-photon spectroscopy and some properties of nonlinear optical processes important for frequency conversion into the deep ultra-violet spectral range are shortly emphasized. In Chapter 3 the motivation for this work is presented in detail, and the applied method for the electric field measurement is further explained and compared with other methods. The experimental set-up is described in Chapter 4 with detailed concepts of the two laser systems and the requirements of two-photon spectroscopy. The results obtained are presented and discussed in Chapter 5.

Chapter 2

Theoretical aspects

2.1 Hydrogen spectrum

Although the hydrogen spectrum is well known, a short overview is repeated here for a better understanding of the Stark spectra presented in this thesis.

Hydrogen is probably the most important of all atoms both for its abundance in the universe and for its theoretical interest. It is the only stable neutral two-body system, and its energy levels can be calculated with a precision far higher than for any other element. In addition, atomic hydrogen possesses a rich spectrum of resonances extending from the radio frequency range to the vacuum ultraviolet and is thus a fertile ground for experimentalists. Because of all these properties the hydrogen atom has been playing a key role in the development and tests of quantum mechanics from its very beginning, including the Dirac theory and quantum electrodynamics as well. As a very suitable tool for metrology it is also used for the determination of fundamental physical constants: with a relative uncertainty well below 10^{-11}, the Rydberg constant, for example, is one of the most accurately known physical constants [15].

The main features of the hydrogen energy level scheme (and thus of the hydrogen spectrum) are obtained by solving the stationary Schrödinger equation

$$H|\Psi_{\mathsf{E}}\rangle = (\frac{p^2}{2m_e} - \frac{e^2}{4\pi\varepsilon_0 r})|\Psi_{\mathsf{E}}\rangle = \mathsf{E}|\Psi_{\mathsf{E}}\rangle \tag{2.1}$$

for an electron (with electric charge $-e$, mass m_e, and momentum p) in the electric field of a fixed, point-like atomic nucleus with electric charge e. The discrete energy eigenvalues of (2.1) which correspond to bound states ($n = 1, 2, 3, \dots$) are:

$$\mathsf{E}_n = -\frac{m_e e^4}{8\varepsilon_0^2 h^2}\frac{1}{n^2}. \tag{2.2}$$

From this, Rydberg's formula of 1889 for the wavenumbers of the hydrogen spectral lines follows immediately:

$$\frac{1}{\lambda_{nn'}} = \frac{\nu_{nn'}}{c} = \frac{\mathsf{E}_n - \mathsf{E}_{n'}}{hc} = \frac{m_e e^4}{8\varepsilon_0^2 h^3 c}(\frac{1}{n'^2} - \frac{1}{n^2}) = R_\infty(\frac{1}{n'^2} - \frac{1}{n^2}), \tag{2.3}$$

where R_∞ is the Rydberg constant (for infinite nuclear mass, see below). As a special case for $n' = 2$, (2.3) implies Balmer's formula of 1885 for the wavelengths of the prominent visible spectral lines of hydrogen belonging to what is now known as the Balmer series:

$$\lambda_{n2} \propto \frac{n^2}{n^2 - 4}. \tag{2.4}$$

As for any spherically symmetrical potential, the eigenstates corresponding to the energy eigenvalues E_n can be chosen to be joint eigenstates $|n, l, m\rangle$ of the Hamiltonian H and the modulus squared $\mathbf{L}^2$ (quantum numbers $l = 0, 1, 2, \dots, n-1$, traditionally designated as S, P, D, ..., and eigenvalues $\hbar l(l-1)$) and the z-component L_z (quantum numbers $m = 0, \pm 1, \pm 2, \dots, \pm l$, and eigenvalues $\hbar m$) of the electron's (orbital) angular momentum. The corresponding wave functions in position space are obtained by separation of the Schrödinger equation in spherical polar coordinates. In contrast to other spherically symmetrical potentials, the corresponding eigenenergies, (2.2), are not only independent of m (the usual "directional degeneracy" found for any spherically symmetrical potential), but also do not depend on the orbital angular momentum quantum number l (the special "accidental degeneracy" of the Coulomb potential proportional to r^{-1}). This is due to the fact that the electron describes closed elliptical orbits without precession in the Coulomb potential. Accordingly, the vector from the center of the potential to the perihelion of the electron orbit, the Runge-Lenz vector, is another constant of the motion, in addition to the orbital angular momentum. The degeneracy of eigenstates with like n, but different l is a consequence of the existence of this additional invariant momentum [16]. As another consequence, an alternative separation of the Schrödinger wave equation can be carried out in parabolic coordinates [11, 17].

Even if the mass M of the hydrogen atom's nucleus is much greater than the electron mass m_e, it is not completely correct to assume that the nucleus does not move at all and the Coulomb potential for the electron thus has a fixed center. Taking the finite mass of the nucleus into account results in the replacement of the electron mass m_e by the reduced electron-nucleus mass μ:

$$\mu = \frac{M \cdot m_e}{M + m_e} \approx m_e(1 - \frac{m_e}{M}). \tag{2.5}$$

Hence, the Rydberg constant R for an actual hydrogen atom is slightly smaller than R_∞ in Equation (2.3). Moreover, the Rydberg constants for hydrogen H (^{1}H) and deuterium D (^{2}H), the "heavy hydrogen" isotope with an additional neutron in the nucleus, are different, and the spectral lines show an isotopic shift in wavelength, say, the relative magnitude of which is about

$$\frac{\Delta\lambda}{\lambda} \approx \frac{m_e}{2M_P} \approx 0.03\% \tag{2.6}$$

($M_P \approx 1836 \cdot m_e$ is the proton mass).

This work is not concerned with the exact absolute values of the frequencies of hydrogen spectral lines, however, but rather with the splitting of these lines under the influence of an applied electric field. Therefore, the effects to be considered in this connection are briefly outlined now.

2.1.1 Fine structure

The Schrödinger equation (2.1) for the hydrogen atom is non-relativistic, assuming that all particle speeds v are completely negligible as compared to the speed of light c. However, for the ground state of hydrogen ($n = 1$), for example, the ratio v/c is of the order of the fine structure constant α,

$$\alpha = \frac{e^2}{2\varepsilon_0 hc} \approx \frac{1}{137}. \tag{2.7}$$

Also, the Schrödinger equation does not take account of the electron's intrinsic angular momentum, the electron spin $\mathbf{s}$, and the magnetic moment connected with this.

The relativistic equation for spin 1/2 particles in a Coulomb potential was first given by Dirac in 1928. In the Dirac theory, the states of the hydrogen atom are described by four-component spinors (instead of the scalar Schrödinger wave function). For electron energies which are much smaller than the electron rest-mass energy $m_e c^2$, two of the four components are negligible as compared to the other two. Neglecting the two "small components", the Dirac equation becomes the two-component Pauli equation. The hydrogen eigenstates of the Pauli equation are found to be simultaneous eigenstates of the modulus squared $\mathbf{l}^2$ of the electron's orbital angular momentum (but no longer of its z-component l_z), of the modulus squared $\mathbf{s}^2$ of the spin angular momentum (but not of its z-component s_z), and of the modulus squared $\mathbf{j}^2$ (quantum number $j = l \pm 1/2 = 1/2, 3/2, 5/2, \ldots$, eigenvalues $\hbar j(j-1)$) and the z-component $j_z = l_z + s_z$ (quantum number $m_j = -j, -j+1, \ldots, j$, eigenvalues $\hbar m_j$) of the total angular momentum $\mathbf{j} = \mathbf{l} + \mathbf{s}$. These angular momentum eigenstates are multiplied by a radial wavefunction which is, up to the order of α^2, the radial wavefunction obtained from the Schrödinger equation.

This makes it easy to construct the Pauli eigenstates $|n,l,j,m_j\rangle$ from the products $|n,l,m;m_s\rangle$ of the Schrödinger eigenstates $|n,l,m\rangle$ and the spin 1/2 eigenstates $|m_s\rangle$ (with $m_s = \pm 1/2$) with the help of Clebsch-Gordan (angular-momentum-coupling) coefficients:

$$\begin{aligned} |n,l,j,m_j\rangle &= \sum_{m,m_s} \langle n,l,m;m_s|n,l,j,m_j\rangle |n,l,m;m_s\rangle \\ &= \sum_{m,m_s} (l,m;\frac{1}{2},m_s|l,\frac{1}{2},j,m_j)|n,l,m;m_s\rangle . \end{aligned} \tag{2.8}$$

The corresponding energy eigenvalues are

$$\mathsf{E}_{nj} = -hcR\frac{1}{n^2}\left(1+\frac{\alpha^2}{n^2}\left(\frac{n}{j+1/2}-\frac{3}{4}\right)\right). \tag{2.9}$$

Equation (2.9) gives the "fine-structure (FS) splitting" of the hydrogen energy levels. The FS splitting removes most of the "accidental" degeneracy of the eigenstates of the Schrödinger equation, but still leaves a degeneracy with respect to $l = j \pm 1/2$.

For the FS splitting within the level n, which is most interesting for this work, one gets

$$\Delta\mathsf{E}_{nj} = \mathsf{E}_{nj} - \mathsf{E}_{n\frac{1}{2}} = hcR\frac{\alpha^2}{n^3}\frac{2j-1}{2j+1} \tag{2.10}$$

for the energy offset from the $\mathrm{nS}_{1/2}$ energy (which equals the $\mathrm{nP}_{1/2}$ energy in this approximation).

2.1.2 The Lamb shift

In 1947 Lamb and Retherford [18] measured a small splitting of the $2S_{1/2}$ and $2P_{1/2}$ levels by means of radio and microwave spectroscopy [19, 20]. This splitting is due to an energy level shift, now generally called Lamb shift (LS), mainly caused by radiative corrections resulting from the interaction of the atomic electron with the quantized electromagnetic field, as first pointed out by Bethe and Brown in 1950 [21]. The present state-of-the-art in the experimental and theoretical determination of the LS is given in [15]. The LS is very nearly proportional to n^{-3}, just as the FS splitting, (2.10). By far the largest effect of this interaction is to lift the $\mathrm{nS}_{1/2}$ energy slightly above the value given by (2.9), which removes the degeneracy of the $\mathrm{nS}_{1/2}$

and $\mathrm{nP}_{1/2}$ states. This effect is of the order of 10% of the fine structure splitting between the $j = 1/2$ and the $j = 3/2$ energies. For other values of l, the degeneracy is also removed, but the corresponding Lamb shifts are about two orders of magnitude smaller, amounting to only about 0.2% of the fine structure separation of the j and $j + 1$ energies.

As an example for the actual magnitude of the FS splitting and the LS, both of which scale as n^{-3}, consider the $n = 2$ level of hydrogen (or deuterium, for which the LS is practically the same). The FS energy separation $\Delta\mathsf{E}_{FS}$ between the $j = 1/2$ and $j = 3/2$ sublevels corresponds to a frequency separation $\Delta\nu_{FS} = \Delta\mathsf{E}_{FS}/h$ of about 11 GHz. In comparison, the $2\mathrm{S}_{1/2}$ vs. $2\mathrm{P}_{1/2}$ LS corresponds to about 1.1 GHz. Nearly 99% of this result comes from the $2\mathrm{S}_{1/2}$ shift, because the $2\mathrm{P}_j$ Lamb shifts correspond to frequency shifts of the order of merely 10 MHz. Because of the proportionality to n^{-3}, the LS values for $n = 3$ are even smaller by a factor of $8/27 \approx 1/3$. Since the laser systems used for two-photon excitation in this work have bandwidths of about 300 MHz at half the transition frequency, they do not at all allow to detect frequency shifts of 100 MHz or below. Therefore, all Lamb shifts except the $\mathrm{nS}_{1/2}$ vs. $\mathrm{nP}_{1/2}$ shift have also been neglected in the calculational results presented below.

2.1.3 Hyperfine structure

The last effect in the hydrogen energy spectrum which has to be considered here is the hyperfine structure (HFS). This is due to the electron's interaction with the nuclear magnetic moment (which is connected with the spin $\mathbf{I}$ of the atomic nucleus). Since the order of magnitude of nuclear magnetic moments is given by the nuclear magneton $\mu_N = e\hbar/(2M_p) = m_e/M_N \cdot \mu_B$, they are distinctly smaller (by a factor of the order of the electron to nucleus mass ratio m_e/M_N) than the magnetic moment of the electron, which is of the order of the Bohr magneton μ_B. In consequence, the HFS splitting is distinctly smaller than the FS splitting and can be calculated in good approximation by first-order perturbation theory, using unperturbed eigenstates of the square of the full atomic angular momentum $\mathbf{F} = \mathbf{j} + \mathbf{I} = \mathbf{l} + \mathbf{s} + \mathbf{I}$ (quantum number $F = |j - I|, |j - I| + 1, \ldots, j + I$) and its z-component $F_z = j_z + I_z$ (quantum number $m_F = -F, -F + 1, \ldots, F$) as well as $\mathbf{j}^2$ and $\mathbf{l}^2$. In full analogy to the construction of the Pauli eigenstates described in Chapter 2.1.1, these states can also be obtained by appropriate angular momentum coupling:

$$\begin{aligned}|n,l,j,F,m_F\rangle &= \sum_{m_j,m_I} \langle n,l,j,m_j;I,m_I|n,l,j,F,m_F\rangle|n,l,j;m_j;I,m_I\rangle \\ &= \sum_{m_j,m_I} (j,m_j;I,m_I|l,j,F,m_F)|n,l,j,m_j;I,m_I\rangle,\end{aligned} \tag{2.11}$$

where $|n,l,j,m_j;I,m_I\rangle$ is the product of the Pauli eigenstate $|n,l,j,m_j\rangle$ and the nuclear spin eigenstate $|I,m_I\rangle$.

For these states, the HFS energy shifts are

$$\mathsf{E}_{HFS} = \frac{\alpha^2 g_N}{n^3}\frac{m_e}{M_N}R\frac{F(F+1)-I(I+1)-j(j+1)}{j(j+1)(2l+1)}. \tag{2.12}$$

They depend on all of the quantum numbers n, l, j, I, and F, and thus remove all of the "accidental" symmetry in the hydrogen energy spectrum. (They do not depend on m_F, of course, because the hydrogen atom as a whole must show the usual directional degeneracy in the absence of an external field.)

According to (2.12), E_{HFS} depends on the nuclear mass M_N and on g_N, the g-factor which multiplies the nuclear magneton in the equation $\mu = g_N\mu_N I$ connecting the nuclear magnetic moment with the nuclear spin. Therefore, and because the nuclear spin is $I = 1/2$ for H and $I = 1$ for D, the HFS splitting is different for hydrogen ($g \approx 5.6$, $M_N = M_p$) and deuterium ($g \approx 0.86$, $M_N = 2M_p$). Since the HFS energy splitting is proportional to n^{-3}, the main HFS effect in the Lyman spectral lines comes from the HFS energy splitting of the lower level. For the hydrogen ground level, the HFS splitting between the $F = 0$ and the $F = 1$ state corresponds to a frequency of 1.42 GHz (the frequency of the famous 21 cm wavelength radiation of radio astronomy). The corresponding HFS splitting of the $2S_{1/2}$ level is only 1/8 of this, namely 178 MHz. For the $2P_{1/2}$ and $2P_{3/2}$ levels, the HFS splittings are still smaller. All the HFS splittings for the $n = 1, 2,$ and 3 levels of hydrogen are listed in the following table.

Table 2.1. shows, that the HFS splittings of the $n = 3$ FS levels is clearly to small to be detected with the laser system used in this work. Therefore, the n = 3 HFS splitting for H has also been neglected in the calculational results presented below. A scheme of hydrogen energy level structure including all mentioned corrections is given in Fig. 2.1.

For deuterium with $I = 1$, the $j = 1/2$ FS levels are split into two HFS sublevels (with $F = 1/2$ and $3/2$), and all other FS levels are split into three HFS sublevels (with $F = j-1, j,$ and $j+1$). The ground level HFS splitting

FS level	HFS splitting (MHz)
$1S_{1/2}$	1420
$2S_{1/2}$	178
$2P_{1/2}$	59
$2P_{3/2}$	24
$3S_{1/2}$	53
$3P_{1/2}$	18
$3P_{3/2}$	7
$3D_{3/2}$	4
$3D_{5/2}$	3

Table 2.1: Hyperfine structure energy splittings of the $n = 1, 2$, and 3 levels of hydrogen.

between the $F = 1/2$ and the $F = 3/2$ state corresponds to a frequency of 327 MHz, and the $2S_{1/2}$ HFS splitting corresponds to 41 MHz. The values for all other HFS splittings are smaller than 15 MHz. Therefore, only the ground level HFS splitting has been taken account in the calculational results presented below.

In summary, the energy of an unperturbed atomic state of hydrogen or deuterium characterized by the quantum numbers: n (principal quantum number), l (electronic orbital angular momentum), $s = 1/2$ (electronic spin angular momentum, omitted here), j (total electronic angular momentum), I (nuclear spin), F (total atomic angular momentum), and m_F ("magnetic" quantum number) can be expressed, to the level of accuracy required here, as a sum of three terms:

$$\mathsf{E}(n, l, j, I, F) = \mathsf{E}_{nj} + \mathsf{E}_{LS}(n, j, l) + \mathsf{E}_{HFS}(n, j, l, F). \qquad (2.13)$$

The first term is the Dirac energy in the Pauli approximation, Equation (2.9), which incorporates the fine structure splitting. The second term is the Lamb shift discussed in Chapter 2.1.2. Its effects can be neglected here, with the exception of the $nS_{1/2}$ vs. $nP_{1/2}$ shift. The last term is the hyperfine splitting, Equation (2.12). For the work presented here, this is important only for the ground level ($n = 1$) of both hydrogen and deuterium, and for the first excited fine structure levels ($n = 2$) of hydrogen.

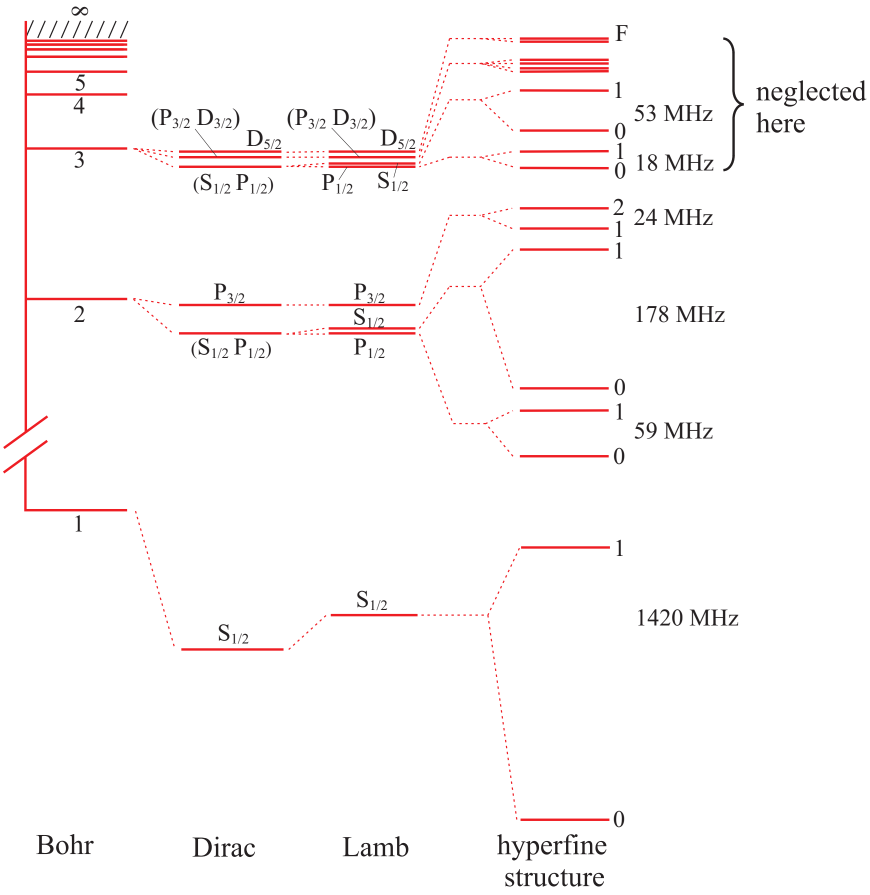

Figure 2.1: Illustration of the eigenstates of the hydrogen atom. The size of the splitting is not at proper scale. From left to right the energy differences always decrease. The important hyperfine splitting values are indicated.

2.2 The Stark effect

Spectroscopic measurements of electric fields are based on the Stark effect. This holds as well for the method examined in this work. A brief discussion of the modifications of the lowest hydrogen energy levels caused by the Stark effect is given in this section.

The influence of electric fields on spectral lines was first studied by J. Stark in 1913 [6]. He measured the spectrum of the Balmer series of hydrogen atoms, emitted from canal rays (Kanalstrahlen) in a region with a high electric field. In the experiment the canal rays penetrating through holes in a cathode plate consisted mostly of neutral particles which were produced by charge exchange from ions accelerated towards the cathode in the extended cathode fall region of a low pressure glow discharge. At a distance of a few mm behind the cathode an additional plane electrode was set to a high dc voltage negative to this cathode. The low pressure below 1 Pa prevented starting of a further discharge in that region and allowed to observe the splitting of hydrogen and helium lines in a constant electric field as high as 10-50 kV/cm.

The theoretical explanation of the Stark effect of the hydrogen atom was one of the first applications of wave mechanics by Schrödinger [11].

As a peculiarity, the hydrogen atom (and hydrogenic ions with only one electron left) shows a linear Stark effect for all excited energy levels in the frame of the Schrödinger equation, i. e., an energy level splitting proportional to the electric field strength E for moderate electric fields. For strong electric fields, quadratic and higher order corrections have to be taken into account, too, in particular for highly excited states. These result from the mixing of levels with different principal numbers. They are completely negligible for the first excited levels, which are energetically well separated from neighboring levels, and for the electric field strengths considered here: for $E = 2$ kV/cm, the largest quadratic correction of the energy corresponds to a frequency of the order of only 1 MHz for $n = 3$, of 100 kHz for $n = 2$, and of less than 10 kHz for the ground state $n = 1$. In comparison, the linear Stark effect for $n = 2$ is of the order of 10 GHz for this field strength.

The linear Stark effect originates from the “accidental” l degeneracy of the $|n, l, m\rangle$ angular momentum eigenstates of the field-free Hamiltonian H (2.1). All other (multi-electron) atoms (and also the hydrogen atom in its ground state) show the usual quadratic Stark effect proportional to E^2, because the electric field is required twice: once to induce an electric dipole moment, and a second time to interact with the dipole. For hydrogen, the angular momentum eigenstates do not have an electric dipole moment as well, but linear combinations $\sum_l a_l |n, l, m\rangle$ can be formed which are eigenstates of H and do have a (permanent) dipole moment even in the limit of $E = 0$ V/cm. Formally, these linear combinations are obtained, for any given n, as the eigenvectors diagonalising (in the subspace of states belonging to n) the interaction energy

$$H^S = -\mathbf{d} \cdot \mathbf{E} = ezE, \tag{2.14}$$

which has to be added to the field-free Hamiltonian H (2.1) for a hydrogen atom in an external electric field (which is homogeneous at least on the scale of atomic dimensions). The Stark splitting of level n is then given by the corresponding eigenvalues of H^S. In the simplest case of the first excited level $n = 2$, for example, there are four angular momentum eigenstates $|n, l, m\rangle = |2, 0, 0\rangle$, $|2, 1, 0\rangle$, $|2, 1, -1\rangle$, and $|2, 1, 1\rangle$, the interaction energy H^S has the four eigenvalues $-3ea_0E$, 0, 0, and $3ea_0E$ (proportional to E), and the corresponding eigenvectors are $(|2,0,0\rangle - |2,1,0\rangle)/\sqrt{2}$, $|2,1,-1\rangle$, $|2,1,1\rangle$, and $(|2,0,0\rangle + |2,1,0\rangle)/\sqrt{2}$.

The treatment of the Stark effect based on the Schrödinger equation, which has been sketched above, is a suitable approximation only if the Stark splitting of the hydrogen energy levels is large compared with the FS splitting. However, this is not true for the conditions considered in this work. By comparison of the unperturbed FS and the linear Stark splitting, the "critical" field strength value for which both effects are about the same is found to be

$$E_c \approx (\frac{10}{n})^5 \frac{\mathrm{V}}{\mathrm{cm}}, \tag{2.15}$$

i.e., 3000 V/cm for $n = 2$ and 400 V/cm for $n = 3$. Since the field strengths in the measurements described below are smaller or have the same order of magnitude, it is obvious that an adequate theoretical treatment of the Stark effect has to include the fine structure splitting.

For weak electric fields, if the Stark effect is small compared to the FS, the problem was first solved by Schlapp [22] and Rojansky [23] in 1928. Starting from the unperturbed energy levels and eigenstates of the Dirac equation, the result they obtained for the first order energy correction, linear in E, is [24]:

$$\mathsf{E}^S = \pm\frac{3}{4} e a_0 E \frac{n}{Z} \frac{|m_j|}{j(j+1)} \sqrt{n^2 - \left(j + \frac{1}{2}\right)^2}. \tag{2.16}$$

Here $a_0 \approx 52.9$ pm is the Bohr radius. It is obvious that the levels with largest j value, $j = n - 1/2$ show no Stark shift in this approximation. The absence of the linear Stark effect for these levels is due to the fact that there are no degenerate levels with neighboring l values. For example, $j = 5/2$ is highest j value of the $n = 3$ level of hydrogen, and there exists only the $\mathrm{D}_{5/2}$ level, but neither $\mathrm{P}_{5/2}$ nor $\mathrm{F}_{5/2}$ which would have the same energy according to the l degeneracy.

As discussed above for the Schrödinger equation, the eigenstates corresponding to the two eigenvalues (2.16) are linear combinations, $(|n, l = j - 1/2, j, m_j\rangle \pm |n, l = j + 1/2, j, m_j\rangle)/\sqrt{2}$ of the unperturbed $|n, l, j, m_j\rangle$ states. Only states with the same m_j can mix in this way. The energy correction (2.16) depends only on the absolute value of m_j. Thus, the new energy levels are at least two-fold degenerate, taking into account both signs of m_j. The electric field cannot remove this degeneracy because the effect of the electric field on a left and right rotating electron with the same time-averaged space distribution is the same. Because of this remaining degeneracy, each unperturbed hydrogenic (n, j) FS level is split into $j + 1/2$ Stark components by the electric field. For weak electric fields, the Stark levels are therefore appropriately designated as fine structure levels with the absolute value of m_j added, e.g., $2\mathrm{P}_{3/2,|m_j|}$, $|m_j| = 3/2, 1/2$.

The analytical results just discussed show how the Stark effect eigenstates evolve from the FS eigenstates if E starts to increase from zero. However, on the one hand the first order perturbation theory is only valid for weak electric fields $E \ll E_c$, and on the other hand the Lamb shift is neglected. In order to overcome these shortcomings, it is advisable to utilize numerical methods. Since the mixing of states with different principal quantum numbers can be safely neglected for the principal quantum numbers n and field strengths E of interest here, all evaluations are done in the finite-dimensional subspace of states belonging to a given value of n, and a straightforward procedure can be applied: In the Pauli approximation, the unperturbed Dirac Hamiltonian H_0 has eigenvalues given by (2.9) or (2.10), the matrix $\langle n, l', j', m_j' | H_0 | n, l, j, m_j \rangle$ is the corresponding diagonal matrix. To account for the Lamb shift, the appropriate correction is applied to the $\mathrm{nS}_{1/2}$ energies. Using the decomposition (2.8), which describes an orthonormal transformation of the basis states, $\langle n, l', j', m_j' | H_0 | n, l, j, m_j \rangle$ is then easily transformed into $\langle n, l', m', m_s' | H_0 | n, l, m, m_s \rangle$. On the other hand, making use of the fact that the electric field does not act on the spin, the matrix of the additional dipole interaction energy H_S is most easily calculated directly as $eE\langle n, l', m', m_s' | z | n, l, m, m_s \rangle = eE\langle n, l', m' | z | n, l, m, \rangle \delta_{m_s', m_s}$ from the well-known formula for the z-matrix elements [17]. Once the H_0 and z matrices have been set up, the eigenvalues and eigenvectors of $H_0 + H_S = H_0 + ezE$ can be obtained with numerical standard procedures of linear algebra for any value of E.

By starting from the diagonal matrix $\langle n, l', j', F', m_F' | H_0 | n, l, j, F, m_F \rangle$ with eigenvalues according to (2.13) and making use of the additional orthonormal transformation given by (2.11), the whole procedure is easily extended to include also the HFS splitting in addition the FS splitting and the Lamb shift. This extended computational procedure has been used [25] to investigate the electric field effects on the HFS splitting of the $n = 2$ level of hydrogen (^{1}H), since this has been found to be at the limit of observability for $E = 0$ V/cm under the experimental conditions of this work (Chapter 2.1.3). Comparing the various HFS frequency shifts against the frequency of the corresponding Stark shifted FS component, only moderate changes (on the 10 MHz level) have been found as the field strength was increased from 0 to 1 kV/cm. In particular, the $2\mathrm{S}_{1/2}$ HFS splitting, which is most interesting because of its magnitude of 178 MHz in the field-free case (Table 2.1), was found to be continuously reduced with increasing field strength and to be only 82 MHz at $E = 1$ kV/cm. Because of this, the HFS splitting of the upper

$n = 2$ and $n = 3$ levels has been completely neglected in the computations used for comparison with the measured spectra.

The only influence on the Stark spectra has the HFS splitting of the ground level which introduces an additional weaker component for each Stark component. The intensity ratio of every weak component (originating from $F = 0$ of the ground state) to the corresponding strong component (originating from $F = 1$ of the ground state) is always 1:3.

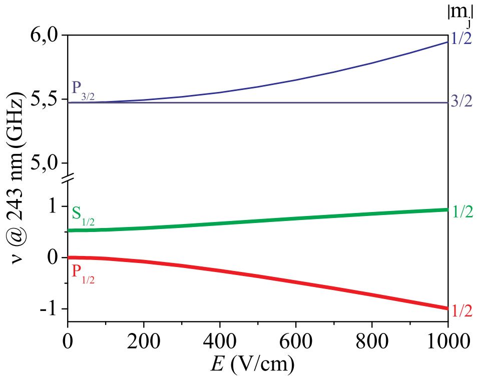

(a) Energy levels are presented as laser frequency offset from the unperturbed $2P_{1/2}$ level.

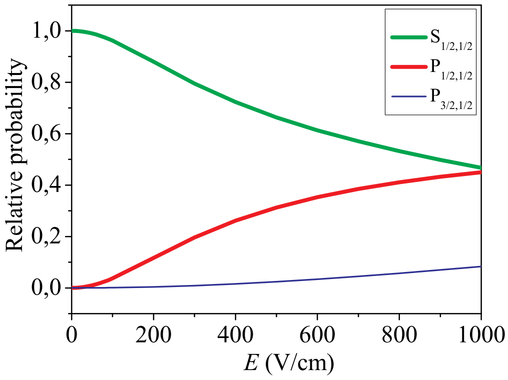

(b) Relative two-photon absorption probabilities for the two linearly polarized laser beams.

Figure 2.2: Stark splitting of the $n = 2$ level of hydrogen as a function of electric field.

For the $n = 2$ and $n = 3$ level considered in this work, Figures 2.2(a) and 2.3(a) show the Stark splitting of the energy levels for the electric field strength values of interest. In addition to the Stark splitting, the relative "transition strengths" for Doppler-free two-photon excitation of the various energy sublevels from the ground state are also shown (see Chapter 2.3). Using the procedure sketched above and (for the transition probabilities) an explicit expression for the two-photon transition operator derived for the hydrogen resonance transitions, the corresponding computations have been done by Seidel [25] with erratum: Ref 7 of [26] and private comunication. The transition probabilities depend on the polarizations of the laser beams used for excitation (also see Chapter 2.3). In Fig. 2.2(b)) the Stark components of the $n = 2$ level excited with two linearly polarized laser beams are presented.

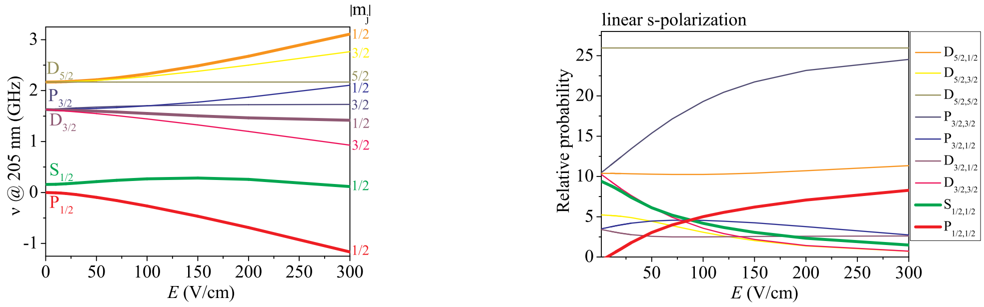

(a) Energy levels are presented as laser frequency offset from the unperturbed $3P_{1/2}$ level.

(b) Relative two-photon absorption probabilities for the two laser beams linearly polarized perpendicular to the electric field.

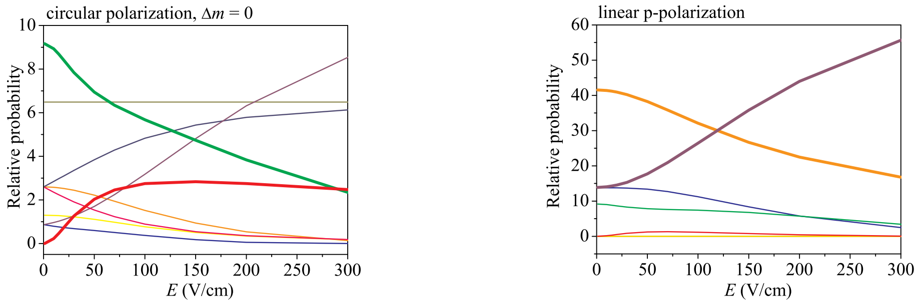

(c) Relative two-photon absorption probabilities for the two laser beams circularly polarized exciting $\Delta m = 0$ transitions.

(d) Relative two-photon absorption probabilities for the two laser beams linearly polarized parallel to the electric field.

Figure 2.3: Stark splitting of the $n = 3$ level of hydrogen as a function of electric field.

With increasing electric field strength, the line strength of the transition to the $2S_{1/2}$ component (the only allowed two-photon transition for $E = 0$ V/cm) decreases, while the originally forbidden transition to the $2P_{1/2}$ component grows due to the level mixing by the electric field. The other forbidden transition to the $2P_{3/2}$ component with $|m_j| = 1/2$ also appears in higher electric fields. The transition to the $2P_{3/2}$ component with $|m_j| = 3/2$ always stays forbidden for two-photon excitation, however, because there is no mixing with any other state of the $n = 2$ level.

In the case of the $n = 3$ level, there are a total of nine Stark components and things are more complex. The line strengths of the Doppler-free two-photon transitions to the various components are shown for the three cases of laser polarization used in this work: both laser beams linearly polarized perpendicular (s-polarization) or parallel (p-polarization) to the electric field, and both beams circularly polarized exciting $\Delta m = 0$ transitions. The results are depicted in Figures 2.3(b), 2.3(c) and 2.3(d), respectively. For circular and s-polarization, Figs. 2.3(b) and 2.3(c), a mixing behavior similar to the one for the $n = 2$ level is important. The originally forbidden transition to the $3P_{1/2}$ component appears and increases account of the transition to the $3S_{1/2}$ component as the electric field strength grows. These two components are clearly separated from the other ones, and their frequency separation, increasing from the Lamb shift at zero electric field, is suitable for determination of the electric field strength value. This method can also be applied for the $n = 2$ level. The Stark components of the other $n = 3$ sublevels originating from $3D_{5/2}$ and $3D_{3/2}$ (the latter degenerate with $3P_{3/2}$), forbidden without field, are hardly separated. Since almost all components of this unresolved manifold have significant intensities in the electric field strength range of interest, Fig. 2.3(b) and 2.3(c), they cannot be easily applied for electric field measurements.

For linear p-polarization, Fig. 2.3(d), the situation is completely different. The originally forbidden transition to the $3P_{1/2}$ component remains very weak in the whole electric field strength range of interest. On the other side, transitions to only two of all the $3D_{5/2}$, $3D_{3/2}$ and $3P_{3/2}$ levels are significant: the transitions to $3D_{5/2,1/2}$, and $3D_{3/2,1/2}$. With increasing electric field strength, the transition probability decreases for the first one and increases for the second one, Fig. 2.3(d). Their frequency separation, Fig. 2.3(a), increases with the field strength from the fine structure value at zero electric field and can be used as a field strength measure.

The components important for the field measurements of this work are emphasized with bold lines in Figures 2.2 and 2.3. The calculated frequency splitting values are used for comparison with the experimentally obtained values.

2.3 Doppler-free two-photon spectroscopy

In emission spectroscopy as well as in single-photon absorption spectroscopy, the Doppler effect sets a significant limit to the spectral resolution. The Doppler broadening is a consequence of the thermal velocities of the observed atoms. Assuming an atom moves with velocity v in its reference frame, the frequency ω of a wave (for example laser photon) with the wave vector $\mathbf{k}$ is Doppler shifted (in the first-order) to

$$\omega' = \omega - \mathbf{k} \cdot \mathbf{v}. \tag{2.17}$$

Due to the Maxwellian distribution of atomic velocities, the emission or absorption spectrum is a Gaussian profile. In the case of a hydrogen atom the Doppler broadening of the Lyman alpha line exceeds the fine structure of the $n = 2$ level already at gas temperatures of about 50 K. Thus for precise measurements the Doppler broadening has to be suppressed by methods of Doppler-free spectroscopy.

If we consider a simultaneous absorption of two photons resonant with the transition between the E_i and the E_f level of an atom we obtain:

$$(\mathsf{E}_f - \mathsf{E}_i)/\hbar = (\omega_1' + \omega_2') = \omega_1 + \omega_2 - \mathbf{v} \cdot (\mathbf{k}_1 + \mathbf{k}_2). \tag{2.18}$$

If the two photons are absorbed out of light waves with equal frequencies $\omega_1 = \omega_2 = \omega$, which travel in opposite directions $\mathbf{k}_1 = -\mathbf{k}_2$, the Doppler shift of the two-photon transition becomes zero. This means that all molecules, independent of their velocities, absorb at the same resonant sum frequency $\omega_1 + \omega_2 = 2\omega$. This effect was first noticed by Vasilenko et al 1970 [27].

A first detailed theoretical treatment of the two-photon processes was given by Göppert-Mayer in 1929 [28]. In general a two-photon absorption can be formally described by a two-step process from the initial level i via a "virtual level" to the final level f. This fictitious virtual level is represented by a linear combination of the wave functions of all real atomic levels k allowed by a one-photon transition from the initial level.

For an atom moving with velocity $\mathbf{v}$ the probability A_{if} for the two-photon transition between the ground state E_i and an excited state E_f, induced by the photons $\hbar\omega_1$ and $\hbar\omega_2$ from two light waves with the wave vectors $\mathbf{k}_1$, $\mathbf{k}_2$, the polarization unit vectors $\mathbf{e}_1$, $\mathbf{e}_2$, and the intensities I_1, I_2 can be written as:

$$\begin{aligned} A_{if} \propto & \frac{\gamma_{if} I_1 I_2}{\left((\omega_{if} - \omega_1 - \omega_2) - \mathbf{v} \cdot (\mathbf{k}_1 + \mathbf{k}_2)\right)^2 + (\frac{\gamma_{if}}{2})^2} \\ & \times \left| \sum_k \frac{R_{ik}\mathbf{e}_1 \cdot R_{kf}\mathbf{e}_2}{\omega_{ki} - \omega_1 - \mathbf{v} \cdot \mathbf{k}_1} + \frac{R_{ik}\mathbf{e}_2 \cdot R_{kf}\mathbf{e}_1}{\omega_{ki} - \omega_2 - \mathbf{v} \cdot \mathbf{k}_2} \right|^2 . \end{aligned} \tag{2.19}$$

The first factor gives the spectral line profile of the two-photon transition of a single moving atom with the natural width γ_{if}. The second factor describes the transition probability. It can be derived quantum mechanically by second-order perturbation theory. This factor contains a sum of products of matrix elements $R_{ik}R_{kf}$ for transitions between the initial state i and intermediate atomic levels k or between this levels k and the final state f. The summation extends over all atomic levels k that are accessible by allowed one-photon transitions from the initial state i including the continuum. The denominator shows, however, that only those levels k, which are not too far off resonance with one of the Doppler-shifted laser frequencies will mainly contribute.

The two-photon transition probability can be understood by another description. In the case of Doppler-free spectroscopy with two photons of equal frequency there is usually no real intermediate level. The distance between the virtual intermediate level, i.e. at half the distance between the initial and the final level, and the nearest real atomic level can be considered as energy defect. Absorbing the first photon, the uncertainty principle allows an atom to remain in the intermediate state only for a time $\Delta t_k \sim 1/\Delta\omega_k$. This time defines the two-photon absorption probability because the absorption of the second photon has to happen within this time. Therefore the higher the energy defect the shorter the time and the smaller the probability for the two-photon absorption. On the other side a fast absorption of the second photon is wanted so that in the meantime no collision can happen to the atom which would change its velocity and destroy the "Doppler-free" condition.

Concerning the selection rules of two-photon transitions, equation (2.19) requires both matrix elements R_{ik} and R_{kf} not to be zero in order to give a non-vanishing transition probability. This means that two-photon transitions can only be observed between two states which are both connected to the intermediate levels by allowed single-photon transitions. Because of the parity changing selection rule for a single-photon transition, the two levels connected by a two-photon transition must have the same parity. This implies the selection rule for the orbital angular momentum change $\Delta l = 0, 2$. Therefore it is possible to reach atomic states, which cannot be populated by a single-photon transition from the initial state. In this respect two-photon absorption spectroscopy is complementary to one-photon absorption spectroscopy.

Since the matrix elements $R_{ik}\mathbf{e}_1$ and $R_{kf}\mathbf{e}_2$ depend on the polarization of the incident radiation, it is possible to select the accessible upper states by a proper choice of the polarization of the laser beams.

In the case of Doppler-free two-photon spectroscopy two counter propagating beams are used with the same intensity and frequency or one beam is reflected into itself. Then the two terms in the second factor of the probability equation 2.19 become identical while the first factor, which describes the line profile, differs for the case when both photons are absorbed out of the same beam. If they come from different beams the probability is twice as large.

The line profile consists of a narrow Lorentzian profile with the natural width γ_{if} corresponding to the Doppler-free signal and a Gaussian profile for the Doppler-broadened background. In the case of equally linear polarized beams the area under the Doppler-profile is half that of the narrow Lorentzian profile. However, choosing a proper polarization of the two laser beams, the background can be completely suppressed. For example if the two counter-propagating circular polarized beams induce the 1s-2s transition, the absorption of two photons out of the same beam is not allowed.

Although the probability of a two-photon transition is generally much lower than that of a single-photon transition, the fact that all atoms can contribute to the signal may outweigh the low transition probability. Because of the low probability which depends on the square of light intensity, the experimental realization of the two-photon absorption became possible only with the development of lasers. The first experiments on Doppler-free spectroscopy were performed in 1974 [29, 30] using sodium atoms. The first Doppler-free excitation of 1s-2s transition of hydrogen was demonstrated for the first time in 1975 [31]. Generally pulsed lasers are used, which deliver sufficiently large peak powers. The spectral line widths of these lasers are often larger than the natural width γ_{if}. In that case the two-photon transition probability decreases slightly and the width of the measured line profile increases to a value larger than the laser bandwidth.

Besides the possibility of Doppler-free spectroscopy the two-photon excitation has other advantages in comparison with a single-photon excitation. The energy gap between the ground state and the excited states of many atomic species correspond to the vacuum ultraviolet (VUV) wavelength range. In the case of one-photon excitation VUV photons are necessary which require experimentally demanding techniques to be generated. Moreover, many of the investigated media will be optically thick for these VUV photons due to the large absorption cross section and high ground-state atom density. In the case of laser induced fluorescence detection, the fluorescent light is sometimes emitted at the same wavelength as the exciting photon, and stray light arising from walls and optical components has to be carefully suppressed. Two-photon excitation schemes overcome these problems. The laser photons at twice the resonance wavelength are in the more favorite ultraviolet (UV) spectral range. Even in the case when the two photon absorption reaches the low-lying levels, the possible fluorescent light is not emitted at the laser wavelength.

Due to all advantages and the strong development of lasers, various Doppler-free laser spectroscopy methods have been developed for different applications in the last thirty years. Some of them are mentioned in Chapter 3.

2.4 Nonlinear optics

The nonlinear interaction of intense radiation with atoms or molecules in crystals or in liquid and gaseous phases is the basis for tunable, coherent sources of radiation with high intensity. These sources, based on different optical mixing techniques which have succeeded in covering the whole spectral range from the VUV up to the far infrared (FIR) are widely applied. The two solid state laser systems providing tunable UV radiation and used in this Ph.D. work are also based on nonlinear frequency conversion processes. For that reason the fundamentals of this processes [32, 33] are given in this chapter.

The usual classical treatment of light propagation inside a medium assumes a linear relationship between the electromagnetic light field and the responding atomic system of the medium. As an oscillatory mechanical device can be overdriven into nonlinear response through the application of large enough forces, an extremely intense beam of light could generate appreciable nonlinear optical effects.

The electric fields associated with light beams from ordinary sources are too small for such a behavior to be easily observable. For this reason the subject had to await the advent of lasers in order that sufficient brute force could cause significant effects in the optical region of the spectrum. Especially pulsed lasers produce high flux densities and accordingly high electric fields.

The electromagnetic field of a light wave propagating through a medium exerts forces on the loosely bound, outer or valence electrons. Ordinarily, these forces are quite small, and in a linear isotropic medium the resulting electric polarization is parallel with and directly proportional to the applied field. In effect, the polarization follows the field.

$$\mathbf{P} = \varepsilon_0 \chi \mathbf{E}, \tag{2.20}$$

where χ is a dimensionless constant known as electric susceptibility. In the extreme case of very high fields, we can expect that P will become saturated, it simply can not increase linearly indefinitely with E. Thus we can anticipate a gradual increase of the ever-present, but usually insignificant, nonlinearity as E increases.

The electric polarization can be written in general as an expansion in powers of the applied field, when the nonlinear susceptibility is taken into account

$$\mathbf{P} = \varepsilon_0 \left(\chi^{(1)} \mathbf{E} + \chi^{(2)} \mathbf{E}^2 + \chi^{(3)} \mathbf{E}^3 + \ldots \right), \tag{2.21}$$

where $\chi^{(k)}$ is the k$^{\mathrm{th}}$-order susceptibility tensor of rank k.

Consider, for example, an electromagnetic (EM) wave

$$\mathbf{E} = \mathbf{E}_1 \cos(\omega_1 t - k_1 z) + \mathbf{E}_2 \cos(\omega_2 t - k_2 z), \tag{2.22}$$

composed of two components incident on the nonlinear medium. The induced polarization at a fixed position (for example, $z = 0$) in the crystal is generated by the combined action of both components. The quadratic term $\chi^{(2)} E^2$ in (2.21) gives the contributions

$$\begin{aligned} \mathbf{P}^{(2)} &= \varepsilon_0 \chi^{(2)} \mathbf{E}^2 (z = 0) \\ &= \varepsilon_0 \chi^{(2)} (\mathbf{E}_1^2 \cos^2 \omega_1 t + \mathbf{E}_2^2 \cos^2 \omega_2 t + 2\mathbf{E}_1 \mathbf{E}_1 \cos \omega_1 t \cos \omega_2 t) \\ &= \varepsilon_0 \chi^{(2)} \left(\frac{1}{2}(\mathbf{E}_1^2 + \mathbf{E}_2^2) + \frac{1}{2}\mathbf{E}_1^2 \cos 2\omega_1 t + \frac{1}{2}\mathbf{E}_2^2 \cos 2\omega_2 t \right. \\ &\quad \left. + \, \mathbf{E}_1 \mathbf{E}_2 \left(\cos(\omega_1 + \omega_2)t + \cos(\omega_1 - \omega_2)t \right) \right), \end{aligned} \tag{2.23}$$

which represents a DC polarization, AC components at the second harmonics $2\omega_1, 2\omega_2$, and terms at the sum or difference frequencies $\omega_1 \pm \omega_2$.

The nonlinear polarization induced in an atom or molecule acts as a source of new waves at frequencies $\omega = \omega_1 \pm \omega_2$ which propagate through the nonlinear medium with phase velocity $v_{ph} = \omega / k = c / n(\omega)$. However the microscopic contributions generated by atoms at different positions in the nonlinear medium can only add up to a macroscopic wave with appreciable intensity if the vectors of the phase velocities of the incident inducing waves and the polarization waves are properly matched. This phase-matching condition can be written as

$$\mathbf{k}(\omega_1 \pm \omega_2) = \mathbf{k}(\omega_1) \pm \mathbf{k}(\omega_2), \tag{2.24}$$

which may be interpreted as momentum conservation of the three photons participating in the mixing process. The phase-matching condition is in principle a vectorial equation, but if the angles between the three wave vectors are too large, the overlap region between the beams becomes too small and the efficiency of the sum or difference frequency generation decreases. Maximum overlap is achieved for collinear propagation of all three waves. In this case $\mathbf{k}_1 \parallel \mathbf{k}_2 \parallel \mathbf{k}_3$ we obtain with $c/n = \omega/k$ and $\omega_3 = \omega_1 \pm \omega_2$ the condition

$$n_3\omega_3 = n_1\omega_1 \pm n_2\omega_2 \Rightarrow n_3 = n_2 = n_1, \tag{2.25}$$

for the refractive indices n_1, n_2 and n_3.

The condition for collinear phase-matching can only be fulfilled if the dispersion, i.e., the dependence of the refractive index $n(\lambda)$ on the wavelength λ can be neglected. This is true for gases and vapors at sufficiently low pressures where $n \approx 1$. The phase-matching in dispersive media can be fulfilled by birefringent crystals, which have two different refractive indices n_o, and n_e for the ordinary and extraordinary waves. While the ordinary index n_o does not depend on the propagation direction, the extraordinary index n_e depends on both the directions of $\mathbf{E}$ and $\mathbf{k}$. The refractive indices values are defined by the three principal axes of the dielectric susceptibility tensor. It is possible to find nonlinear birefringent crystals where the phase-matching condition (2.25) for collinear phase-matching can be fulfilled if one or two of the three waves propagate as extraordinary wave and the rest as ordinary wave through the crystal in a direction θ, given as angle between the optical axis of the crystal and wave vector $\mathbf{k}$.

2.4.1 Second harmonic generation

For the case $\omega_1 = \omega_2 = \omega$ from two photons with equal frequencies, double the input frequency is generated in a nonlinear medium. This frequency doubling or second harmonic generation (SHG) is a special case of sum frequency generation. The phase-matching condition (2.24) becomes

$$k(2\omega) = 2k(\omega) \Rightarrow v_{ph}(2\omega) = \frac{2\omega}{k(2\omega)} = \frac{2\omega}{2k(\omega)} = v_{ph}(\omega), \tag{2.26}$$

which implies that the phase velocities of the incident and second harmonic (SH) wave must be equal. This can be achieved in a certain direction against the optical axis if in this direction the extraordinary refractive index $n_e(2\omega)$ for the SH wave equals the ordinary index $n_o(\omega)$ for the fundamental wave in a negative birefringent uniaxial crystal. The polarization direction of the SH wave is orthogonal to that of the fundamental wave.

In practice, some phase mismatch is always present, namely $n(\omega)$ is slightly different from $n(2\omega)$. This affects the intensity of SH wave, which is given by

$$I(2\omega, L) = I^2(\omega)\frac{2\omega^2\left|\chi_{eff}^{(2)}\right|^2 L^2}{n^3c^3\varepsilon_0}\frac{\sin^2(\Delta kL)}{(\Delta kL)^2}, \tag{2.27}$$

ΔkL is the phase difference at the end of a nonlinear crystal with length L, $\chi^{(2)}_{eff}$ is the effective nonlinear coefficient, dependant on the nonlinear crystal parameters and the propagation direction. If the length L exceeds the coherence length

$$L_{coh} = \frac{\pi}{2\Delta k} = \frac{\lambda}{4(n(2\omega) - n(\omega))}, \tag{2.28}$$

the fundamental wave and the SH wave come out of phase, and destructive interference begins which diminishes the amplitude of the SH wave. The difference $n(2\omega) - n(\omega))$ should therefore be sufficiently small to provide a coherence length larger than the crystal length L. In other words, the crystal length should be maximal possible for a given coherence length to provide higher SH intensity, see equation (2.27).

If the wavelength of the pump laser is tuned, the phase-matching can be maintained either by turning the crystal orientation against the pump beam propagation or by controlling the temperature, which relies on the temperature dependence of the refractive index. If the laser light propagates in the direction with some angle to the phase-matching direction, the conversion efficiency, defined as $I(2\omega)/I(\omega)$, will reduce dramatically. The acceptance angle given as the full angle at half maximum of the conversion efficiency curve is a specific parameter for each type of nonlinear crystal and depends on the wavelength of the pump beam. According to this value, a proper crystal for some nonlinear process should be chosen taking into account the divergence of the pump beam. In some cases the acceptance angle is large enough to provide a small wavelength tuning without changing the orientation of the crystal.

2.4.2 Sum frequency generation

The general case of summing two different frequencies, sum frequency generation (SFG) is often more advantageous than frequency doubling. Since the intensity of the generated radiation is proportional to the product of the intensities of the two input waves, an intense output can be achieved with one input from a selected powerful laser source, while the other one is chosen to match the desired frequency. The range that can be covered by sum frequency generation is generally wider than accessible with SHG. Especially radiation at wavelengths too short to be produced by frequency doubling can be generated by mixing two different frequencies ω_1 and ω_2. The lower wavelength limit for nonlinear processes in crystals is generally given by the absorption (transmission cut-off) of the crystals. The lowest cut-off have

β-BaB_2O_4 (BBO) crystals: they are transparent down to 190 nm, but SHG has its phase matching limit already at 205 nm.

The generation of higher harmonics is also achieved with sum frequency generation. For example the third harmonic is generated as the sum of the SH and the fundamental. The fourth harmonic could be generated by frequency doubling the SH. But in many cases a sequence of SFG processes is more efficient, namely second, third and finally the fourth harmonic as the sum of the third harmonic and its fundamental. Such a concept has been applied for the development of the solid state laser system at 205 nm. The 820 nm output from a seeded optical parametric oscillator is amplified and transformed into its fourth harmonic. The common idea would be to double twice the 820 nm radiation, obtaining in the first step 410 nm and then 205 nm radiation. But the effective nonlinear coefficient for frequency doubling the 410 nm radiation in a BBO crystal is very low, because of the unfavorable phase-matching condition. Since the conversion efficiency is quadratically dependent on the nonlinear coefficient, equation (2.27), it is much more efficient to use three sum frequency processes. The 820 nm radiation is frequency doubled in a first BBO crystal, then it is summed with the second harmonic at 410 nm to the third harmonic at 273.3 nm which is finally summed again with the fundamental at 820 nm resulting in the desired 205 nm radiation. The effective nonlinear coefficients of the last two processes are about one order of magnitude larger than simple frequency doubling the 410 nm radiation.

2.4.3 Optical parametric oscillator

An optical parametric oscillator (OPO) is based on the parametric interaction of a strong pump wave $E_p \cos(\omega t - \mathbf{k}_p \mathbf{r})$ with the molecules in a crystal with a sufficiently large nonlinear susceptibility. This interaction can be described as an inelastic scattering of a pump photon $\hbar\omega_p$ by an atom or a molecule where the pump photon is absorbed and two new photons $\hbar\omega_s$ and $\hbar\omega_i$ are generated. Because of the energy conservation, the frequencies ω_s and ω_i are related to the pump frequency ω_p by

$$\omega_p = \omega_i + \omega_s. \tag{2.29}$$

Analogous to the sum-frequency generation, the parametrically generated photons can add up to a macroscopic wave if the phase-matching condition

$$\mathbf{k}_p = \mathbf{k}_i + \mathbf{k}_s, \tag{2.30}$$

is fulfilled. This may also be regarded as the conservation of momentum for the three photons involved in the parametric process. In other words, parametric generation splits a pump photon into two photons that satisfy conservation of energy and momentum at every point in the nonlinear crystal. For a given wave vector $\mathbf{k}_p$ of the pump wave, the phase-matching condition (2.30) selects, out of the infinite number of possible combinations $\omega_i + \omega_s$ allowed by (2.29), a single pair which is determined by the orientation of the nonlinear crystal with respect to $\mathbf{k}_p$. The resultant two macroscopic waves are called signal and idler wave with $\omega_s > \omega_i$. The most efficient generation is again achieved for collinear phase matching, where all three wave vectors are parallel.

If the nonlinear crystal pumped by the incident wave is placed inside a resonator, the oscillation on the idler or signal frequencies can start when the gain exceeds the total losses. The optical cavity may be resonant for both the idler and the signal waves or for only one of them. The bandwidth of the OPO depends on the parameters of the resonator, on the line width of the pump laser, on the pump power and the wavelength. It is difficult to generate narrow bandwidth output from an OPO while maintaining high output energy and good pump conversion efficiency. One possibility is to use disperse elements inside the resonator e.g. a grazing-incidence grating (applied in the 243 nm laser system) or a tilted etalons. This requires complex techniques to retain single-mode operation while the system is tuned. Another approach is to use the technique of injection seeding with a continuous wave (cw) or pulsed laser. Injection seeding with a narrow bandwidth laser on or near a cavity resonance and pumping the seeded resonator with a single-mode laser provide sufficient conditions for the oscillation on a single longitudinal mode of the OPO resonator. If the resonator is maintained at resonance with the seeded frequency, the tunability of the seed laser may be exploited to control the signal and idler frequencies. Using a cw source to seed, conventional cw methods may be applied to provide stabilization even of a pulsed OPO (this method is used for the 205 nm laser system).

The damage threshold is an important crystal parameter that should be taken into account while designing a nonlinear system. It depends on the irradiance, the wavelength, the pulse duration and the beam profile of the pump and the generated beams. Relatively new nonlinear crystals like $KTiOPO_4$ (KTP), BaB_2O_4 (BBO) and LiB_3O_5 (LBO) are widely used in the last ten years, because they are very suitable for OPO's due to their large nonlinear coefficient in combination with a high damage threshold.

The utilization of optical parametric oscillators for the generation of widely tunable narrow-band pulsed radiation with a high peak power has made them a very powerful tool in high resolution laser spectroscopy.

Chapter 3

Method for electric field measurements

A short summary of the various laser spectroscopic methods applied for the electric field measurements is given here together with the motivation for this Ph.D. work.

Laser spectroscopy has been developed in the last twenty years and can also be applied for electric fields studies in plasmas. In general, laser techniques can be non-perturbing when the laser has a short pulse duration and a moderate power. Furthermore, these methods offer a nanosecond time resolution, a sub millimeter spatial resolution and a precise spectral selectivity. Their versatility can be seen by the wide parameter range in which they have been used. Electric fields from a few volts per centimeter to more than 10^6 V/cm were measured in discharges with current densities ranging from μA/cm^2 to more than A/cm^2. The discharges were operated dc or up to few MHz, as well as in pulsed mode. In addition to electric field strengths determination, laser spectroscopic methods can be used to measure densities of different species in plasmas, atomic or molecular translational temperatures or non thermal distributions.

Electric fields are optically determined from the Stark effect, which introduces changes in the structure of atomic or molecular spectra. These changes include the appearance of forbidden components, shifting and mixing of components and/or changing of their intensities. Depending on the magnitude of the effect and the resolution of the experiment, individual components of interest or only the broadening of the whole spectrum can be observed. Measured data are compared with theoretical values if available, or with values obtained by calibration with known electric fields. Using laser photons, measured species are excited from the ground state or from a long living metastable state usually to a selected field sensitive Rydberg state. The drawbacks of Rydberg states are their long lifetimes and their unfavorable branching ratios that inhibit the direct observation of fluorescence light.

Helium atoms are often used as field sensitive spectators because the Stark effect can be easily calculated. The final state is mostly the $n = 11$ Rydberg state [34, 35], but even higher states like $n = 26 - 46$ are possible for a better field sensitivity. In the latter case, however, only broadening or series termination of Rydberg spectra can be observed [36, 37]. Instead of optogalvanic detection, laser induced fluorescence has been applied to increase the spatial resolution. Fluorescence can be observed from a state by depopulating the Rydberg level by collisions [38, 39, 40, 41] or by deexcitation with an additional laser [42]. In the case of higher electric fields, lower levels of He like $2^1P - 3^1D$ yield field strengths straightforward from frequency shift measurements [43]. Using the polarization change of fluorescent light, a quite different method for electric field measurement has been proposed suitable for the edge of tokamak plasmas [44, 45]. Measurements are also performed with Ar atoms and calculated [46, 47] or calibrated field values [48, 49, 50] for comparison. Hetero-nuclear diatomic molecules, like BCl [51, 52], NaK [53, 54, 55, 56] and BH [57] have also been used as a probe.

The hydrogen atom is probably the most prominent candidate for an electric field probe. Its excited levels are highly sensitive to electric fields, the theory of its Stark splitting has been well known since long [24, 58] and it is anyway present in many plasmas of industrial interest. Several different measurement techniques for atomic hydrogen have been published. For instance, Doppler-free laser polarization spectroscopy [59] was demonstrated by the Stark splitting of the hydrogen Balmer beta line. The Stark structure of the Lyman alpha was studied with a pulsed VUV laser system [60]. 2+1 photon excitation [13] to the $n = 6$ level was observed by indirectly induced Balmer alpha fluorescence. The electric field dependence of the $n = 6$ Stark spectra was obtained by calibration with known field values. The most sensitive method for electric field measurement with hydrogen was developed by Czarnetzki et al. [12]. They used first a Doppler-free two-photon excitation to the $n = 3$ level, and then observed the decrease of the Balmer alpha fluorescence by depopulating the $n = 3$ level with an additional IR-laser exciting Rydberg states. A high field sensitivity was obtained by tuning the IR laser across Rydberg states. Electric fields down to 5 V/cm could be deduced from the comparison of the measured and the calculated spectra taking into account the Stark effect of the $n = 3$ and the Rydberg levels. Using this method and a method proposed for He by Greenberg and Hebner [38], they were able to calculate a number of parameters from spatial and temporal electric fields distributions, like net-charge, the ion density and energy distribution, sheath voltage and displacement current in the sheath region of a capacitively coupled rf GEC reference cell [2, 3]. Another two methods for electric field measurements were published recently. One method uses two-photon polarization spectroscopy of the Stark split $n = 2$ level of deuterium [61] and the other observes the two-step-resonant excited Stark spectra of the $n = 8$ level of hydrogen [57].

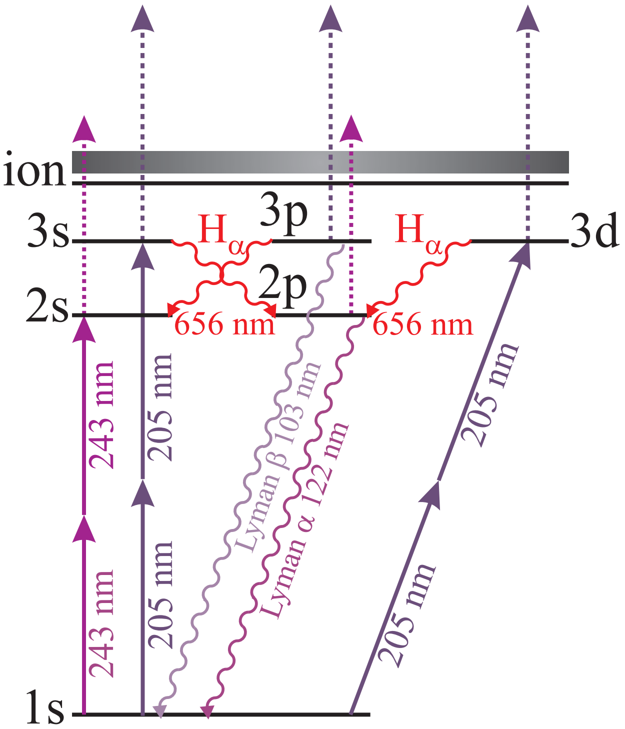

Figure 3.1: First three levels of atomic hydrogen with connecting two-photon laser excitation and possible fluorescence transitions.

The scheme with two laser photons at 205 nm exciting hydrogen atoms from their ground level to the $n = 3$ level followed by observation of the induced Balmer alpha emission, Fig. 3.1, gives the largest number of fluorescence photons per incident laser photon in comparison with other schemes [62]. Reported for the first time by Bokor and co-workers [63], this scheme was applied for hydrogen atom density measurements in different plasma sources and flames [64, 65, 66, 67, 68, 69]. Doppler-free two-photon excitation [70] was also used for the investigation of the collisional broadening in flames [71] and for the experimental and computational study of the time profile of fluorescence light emission [72] in an expanding plasma.

Booth et al. [14] proposed this scheme for electric field measurements by observing the Stark splitting of $n = 3$ level of hydrogen atom. In the

transition	resonance wavelength (nm)	laser wavelength (nm)
$1S_{1/2}$-$2S_{1/2}$	121.56731	243.13462
$1S_{1/2}$-$3S_{1/2}$	102.57228	205.14456
$1S_{1/2}$-$3D_{3/2}$	102.57218	205.14436
$1S_{1/2}$-$3D_{5/2}$	102.57214	205.14428

Table 3.1: Wavelengths of the resonance and the laser for two-photon excitation of the first two excited levels of atomic hydrogen. The values are given in nm for vacuum wavelengths. The five digits after the decimal point correspond to the 0.05 pm precision of our pulsed laser.

experiment, a complex tunable laser system was applied. It consisted of a cw ring dye oscillator pumped by an Ar^+ laser, a series of pulsed dye amplifiers pumped by the second harmonic of a Q-switched Nd:YAG laser and a frequency tripling unit. The laser beams at 205 nm were linearly polarized parallel to the external electric field. But according to theory, the authors assumed a better sensitivity with the laser beams polarized perpendicular to the field.

The aim of this Ph.D. work was to explore further the possibilities of electric field measurements with the Stark spectra of the low excited $n = 2$ or 3 levels of hydrogen, taking advantage of precisely tunable laser systems with a nanosecond pulse duration and a nearly Fourier-limited bandwidth. Developed for high resolving Doppler-free two-photon spectroscopy in our laboratory, these solid-state laser systems have a bandwidth of about 300 MHz down to a wavelength of 200 nm. This corresponds to a relative spectral resolution of $5 \cdot 10^6$.

According to the selection rules, two-photon transitions require a change of the atomic angular momentum $\Delta l = 0$ or 2. From the 1s ground state of atomic hydrogen, only the 2s level can be excited with two laser photons at 243 nm (1s-2s transition), or the 3s or 3d level with two photons at 205 nm (1s-3s/d transition), see Fig. 3.1. The laser wavelengths at twice the values of the resonant transitions are given here approximately as whole numbers in nm. This notation is used for convenience in the whole thesis; more exact values of the resonant transitions with the corresponding laser wavelengths are given in Table 3.1.

The measurements have been performed in a hydrogen cell were the hydrogen molecules are thermally dissociated by a hot filament, see Chapter 4.1. Hydrogen atoms are excited by two counter-propagating laser photons to obtain Doppler-free Stark spectra. Some of the excited atoms decay radiatively to lower states by the emission of a fluorescence photon. As this radiation is used to detect the two-photon laser excitation, this is a laser induced fluorescence method (LIF). Sometimes the acronym TALIF can be found in the literature for the two-photon (absorption) laser induced fluorescence, but in this work, the well-known LIF acronym is used exclusively.

Concerning the fluorescence radiation starting from the $n = 3$ level, there are two lower levels. Balmer alpha photons at 656.28 nm and Lyman beta photons at 102.57 nm could be emitted, see Fig. 3.1. However, Lyman beta can only occur from the 3p level, which is not directly populated by the two-photon excitation, but only by collisional transfer or by level mixing in external electric fields. In contrast, Balmer alpha radiation is possible from any $n = 3$ sublevel, in particular directly after the two-photon excitation. Anyway, the visible part of the fluorescence spectrum like Balmer alpha is much more convenient for detection and has been used.

A similar situation holds for the $n = 2$ level. In the unperturbed field-free case, only the “metastable” 2s sublevel is excited by two-photon absorption from the 1s ground state and Lyman alpha radiation at 121.57 nm can be emitted only from 2p levels. As light in the vacuum ultra violet spectral range it is quite complicated for detection and only suitable in very special cases such as fusion plasma diagnostics [73, 74]. In the frame of this Ph.D. work the detection of Lyman alpha radiation was not performed. Instead, another detection method concurrent to the fluorescence is used. The excited hydrogen atoms are partly ionized by the absorption of a third photon from the exciting laser pulse, a nonlinear three photon process, which is enhanced by the two-photon resonance. The produced charged particles are separated by the applied electric field and the ions are collected by a pick-up wire, see Chapter 4.1. This charge pulse extracted from the wire is measured as optogalvanic signal (OG).

The cross section for photo ionization of level n for hydrogen atom is given as a function of the frequency ν of the laser photon [75]:

$$\sigma_n^{el}(\nu) = 2.815 \cdot 10^{29} cm^2 s^{-3} \frac{1}{\nu^3 n^5} \tag{3.1}$$

According to (3.1), the laser induced ionization of the $n = 2$ level with 243 nm photons has a probability more than ten times higher than ionization of the $n = 3$ level with 205 nm photons. The process can produce a significant number of ions and electrons, which is sometimes unwanted because this can perturb the measurements, by collisional depopulation or a decrease of the fluorescence signal. For that reason a moderate laser intensity should be used [72].

We have applied OG detection for the Stark spectra of $n = 2$ level, while in the case of $n = 3$ level spectra LIF and OG signals are recorded simultaneously. LIF detection has the advantage of an improved spatial resolution, see Chapter 4.5. Besides, it is a pure optical method without additional demands like electrodes for charged particles detection, which can not be fulfilled in all plasma sources.

The Stark splitting scales quadratically with the principal quantum number, thus the $n = 3$ level shows a pronounced field sensitivity in comparison with the $n = 2$ level and makes more precise electric field measurements possible. For that reason the measurements of the $n = 3$ Stark spectra are the main point of this Ph.D. work. The approach of Booth et al. [14] has been investigated in detail by comparing the LIF spectra with the OG spectra and by the extension to altogether three laser polarizations. The measurements are performed with two laser beams linearly polarized perpendicular to the external electric field, named s-polarization, linearly polarized parallel to the field, named p-polarization, and circularly polarized in opposite directions to excite $\Delta m = 0$ transitions. Not depending upon the direction of the external electric field the circular polarization is convenient for applications where the field direction is unknown or variable.

The idea of exploring this method is to define, for each laser polarization, a single field sensitive parameter of the two-photon absorption spectrum that can be easily used for electric field determination. The frequency shift between two Stark components is preferred rather than the intensity ratio influenced not only by the two-photon absorption probability but by additional effects as well. If the Stark components are well isolated in the measured spectrum their frequency shift is easy to compare with values from the calculated Stark spectra. Due to the Stark splitting and mixing at non-vanishing electric fields, the forbidden p component appears in the spectrum. Increasing from the Lamb shift, the shift between the $S_{1/2}$ and the $P_{1/2}$ component is anticipated as a particularly suitable parameter for a sensitive electric field determination. To resolve this shift at low electric fields, a tunable laser with a narrow bandwidth is needed for the two-photon excitation.

It should be pointed out that the simplicity of the proposed method lies in the necessity of only a single laser excitation and the observation of clear Stark spectra of the $n = 2$ or $n = 3$ level of hydrogen. Compared with methods using Rydberg levels, the field sensitivity seems to be low. Nevertheless this method is meant to measure preferentially external electric fields and it should provide sufficient sensitivity for field values that are significant for plasma processes. These requires field strengths of at least few tens of V/cm.

Chapter 4

Experimental set-up

4.1 Hydrogen cell

The measurements were performed in a small vacuum cell filled with hydrogen gas at 300 Pa. The cell housing is made of aluminum covered with water-cooled brass flanges Fig. 4.1. The hydrogen molecules are thermally dissociated at the hot surface of a filament 1.5 mm in diameter, electrically heated to a temperature of about 2000 K. For the first measurements, a tantalum filament was used heated with a current of 80 A dc. As the produced hydrogen atoms modified the tantalum texture, the wire had a short lifetime of about 2-3 hours under the measuring conditions. As a consequence the efficiency of the atomic hydrogen production was decreasing during the whole operating time reducing the measured signal as well. Because of the low dissociation efficiency, the LIF signal was very weak during the first measurements also. This problem was solved by replacing the tantalum filament with a tungsten filament of the same diameter heated to about the same temperature with a current of 90 A dc. This has considerably increased the possible measuring time and the signal intensity.

The kinetic temperature of the hydrogen atoms in the measuring volume at a distance of several mm from the filament is about $T = 500$ K (see Chapter 5.1.1). This estimate of the gas temperature at a pressure of 300 Pa yields a total particle density of atomic and molecular hydrogen $n \sim 5 \cdot 10^{22}$ m^{-3} using the ideal gas equation $p = nkT$, where k is the Boltzmann constant. It is known that the dissociation degree does not exceed 1% [67]. In this case, the mean free path of a hydrogen atom is in the order of 100 μm. This can explain the low temperature of hydrogen atoms, because on their way from the filament to the measuring volume hydrogen atoms experience more than ten collisions with cold hydrogen molecules, which are at room

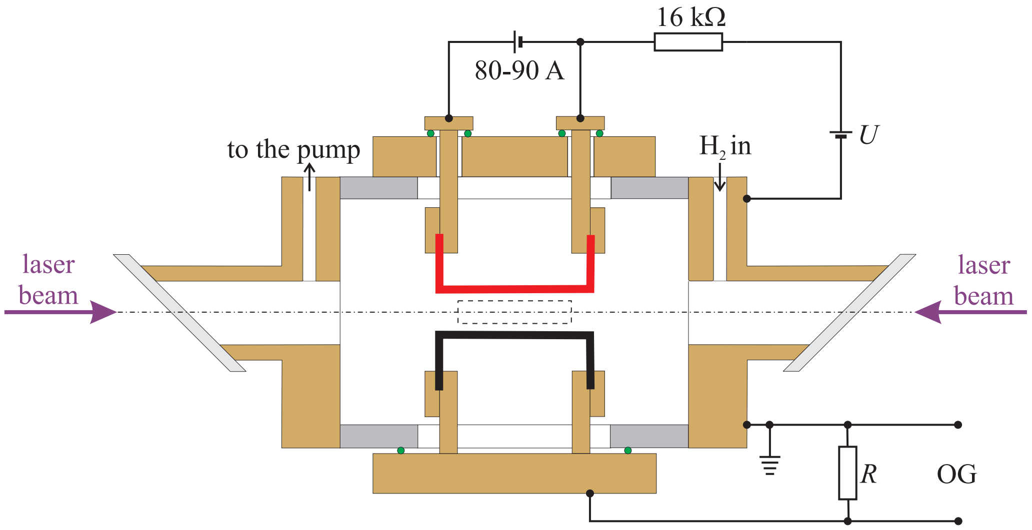

Figure 4.1: Schematic sectional drawing of the hydrogen cell made of an aluminium housing (gray color) covered with water-cooled brass flanges (gold color). The electric field between the hot filament (red line) and the pick-up wire (black line) is established by applying a variable dc voltage U of up to 300 V through a 16 kΩ load resistor. The fluorescence signal is observed through a window on the back side of the cell (dashed rectangle). The current flow from the pick-up wire, through the resistor R, to the ground level is detected as optogalvanic signal (OG).

temperature due to the water cooled walls of the hydrogen cell. For such strong temperature gradients the atomic density is only a rough estimate.

Besides the power supply for heating, the filament is connected to an adjustable positive dc high voltage, across a 16 kΩ resistance. Together with an additional grounded wire, made of tantalum, 1.5 mm in diameter, and mounted in parallel at a distance of about 8 mm (the distance is 3 mm for the measurements at 243 nm), this voltage defines the electric field, see Fig. 4.1. The two counter propagating laser beams pass at half the distance between the wires, where the electric field inhomogeneity is less pronounced. The ions and electrons produced by absorption of a third laser photon are separated by the applied electric field. The ions are collected by the pick-up wire and the resulting current pulse is detected as it flows to the ground level of the high voltage power supply. The optogalvanic signal is measured as voltage drop across a resistor (R).

On one side of the cell there is a window, indicated as dashed rectangle in Fig. 4.1, for observation of the laser induced fluorescence signal perpendicular to the electric field and to the laser beam. In this direction a slit aperture is mounted inside the cell at the height of the laser beams. This reduces the background light from the hot filament in the fluorescence detection channel.

The laser beams are entering the hydrogen cell through uncoated UV grade fused silica windows mounted at Brewster angle with respect to the linear polarization of the laser beams in the case of the p- and s-polarization. In the case of circular polarization, the windows are mounted at 1° angle of incidence in order not to disturb the circular polarization of the laser beams while entering the hydrogen cell. The small angle prevents reflected beams inside the cell from hitting one of the wires.

4.2 Laser system at 243 nm

For Doppler-free two-photon excitation of the 1s-2s transition of hydrogen atoms, a narrow bandwidth UV laser tunable at 243 nm is necessary. Because of the small transition probability for two-photon processes, high irradiances of about 100 MW/cm^2 are needed. Since no available commercial system could fulfill these demands of pulse intensity and spectral quality, this laser system was developed in our group about ten years ago. At a repetition rate of 10 Hz, it delivers typically 10 mJ of pulse energy with 2.5 ns pulse duration. The tunability of the system opens up the possibility for two-photon spectroscopy of other atomic species like oxygen (225.8 nm), nitrogen (211 nm) and carbon (280.4 nm).

The concept of the laser system [76] is to use the second and the third harmonic of a Nd:YAG laser for the creation of tunable, pulsed UV-radiation by frequency splitting in optical parametric processes and by sum frequency generation. For this purpose tunable radiation with a narrow bandwidth is produced in the near infrared region, amplified and then converted into the UV, Fig. 4.2 and Fig. 4.3.

The laser system contains a Continuum Mirage 500 system commercially available at that time. It consists of a tunable single-mode optical parametric oscillator (KTP-OPO) and an optical parametric amplifier (BBO-OPA), which are pumped with the second and the third harmonic of a pulsed, injection-seeded single-mode Nd:YAG laser (Continuum Powerlite 9010). The original tuning range is from 430 nm to 2120 nm. To generate such a wavelength, the fixed frequency second harmonic of the Nd:YAG laser at 532 nm is split into signal and idler wave by the KTP-OPO operated single longitudinal mode, for example into tunable beams at wavelengths 772 nm and 1711 nm. In a second frequency splitting process either the signal or the idler wave is amplified in the BBO-OPA pumped with the third harmonic of Nd:YAG.

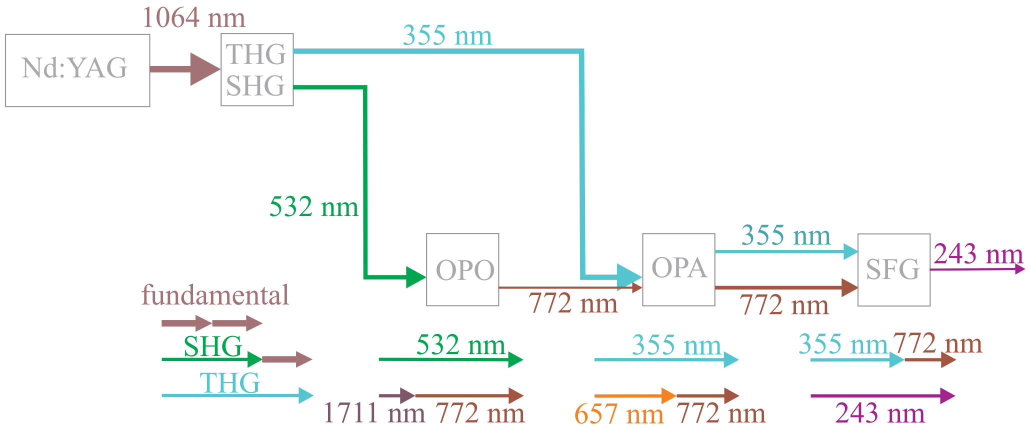

Figure 4.2: Principle of the 243 nm laser system. A chain of five nonlinear processes is used to transform the fix frequency infrared radiation of an injection seeded Nd:YAG laser into tunable UV radiation.

According to the PTB concept this system could be extended in an unusual manner to produce UV radiation either from signal or idler wave of the OPA simply by mixing with the leftover of its third harmonic pump beam in a sum frequency generation process in an additional BBO crystal. By this way the wavelength range from 205 nm to 300 nm can be covered. Since the third harmonic is used a second time in the final sum frequency generation process, the whole chain of non-linear processes had to be optimized for a high conversion efficiency concerning not only the preparation of the third harmonic beam but also the signal and the idler beam from the OPO.

This optimization and beam preparation of the Mirage 500 system, according to a pending PTB patent, as well as mounting the sum frequency generation part inside its original housing were performed in our laboratory.

4.2.1 Optimization of the laser system

For two-photon spectroscopy, not only a high irradiance and narrow bandwidth but also a high pulse to pulse stability is necessary. Since the commercial system did not have sufficiently good performance, some modifications were needed leading to a better pulse stability.

The OPO uses a short resonator (7.75 mm optical length) for its signal with a grazing incidence grating in a Littman configuration, Fig. 4.4. While the pump beam is coupled in and the OPO output beam is coupled out of the resonator via the zero order of the grating, its first order is used to couple back the signal into the resonator by a tuning mirror. This mirror as well as the KTP-OPO crystal are rotated for tuning. The OPO pulse

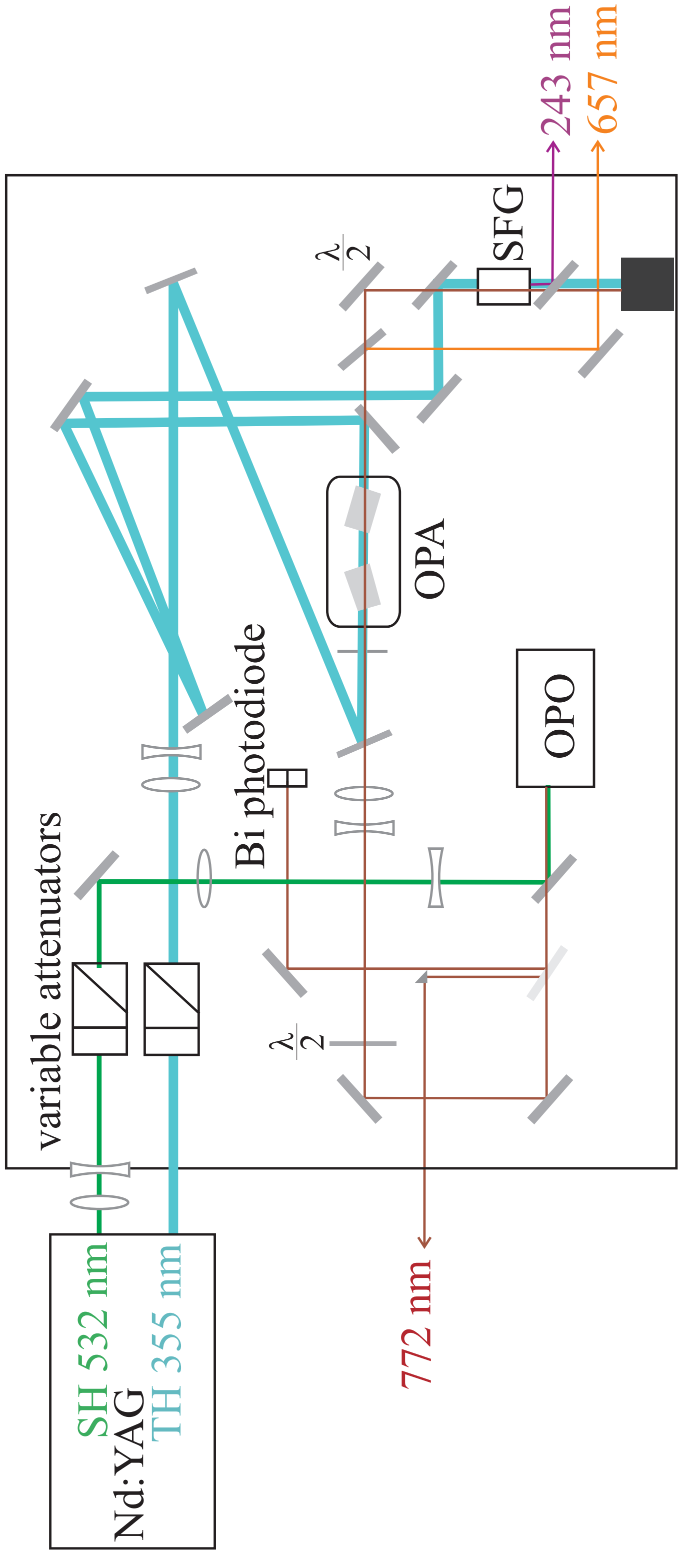

Figure 4.3: Scheme of the improved Mirage 500 with the added sum frequency generation.

output is highly sensitive on the direction, the position, the beam profile and the frequency of the pump beam. As described by the pending patent, the pump beam profile is modified from round to elliptical more extended in the horizontal direction leading to a better pulse stability. This crucially enhances the single-mode operation and facilitates the stabilization of the direction of the OPO beam by observing its beam profile on a split-photodiode and adjusting the resonator length through a translation of the back mirror. To check alignment and wavelength scanning, the spatial profile is observed by a CCD camera and the time structure of the output pulse is monitored with a fast photodiode.

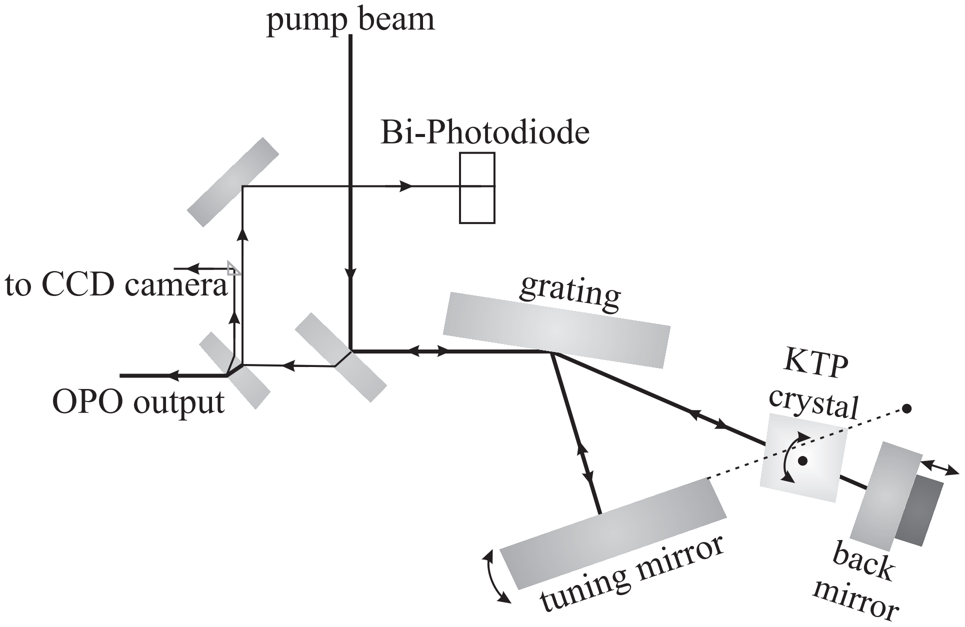

Figure 4.4: Scheme of the OPO resonator inside the Mirage 500.

The OPO signal and the third harmonic beam are both resized with telescopes for an optimal amplification in two back-to-back BBO-OPA crystals, Fig. 4.3. A high irradiance of the third harmonic close to the crystal surface damage limit is wanted for an efficient signal amplification by the parametric process. On the other side, strong focusing leads to a high divergence of both the third harmonic and the amplified signal beam unwanted for the final sum frequency generation with small acceptance angle. For that reason, the third harmonic beam is only slightly reduced with a telescope and the central part of the beam is selected by a teflon aperture in front of the first BBO crystal. In that way a safe operation of the BBO crystals is provided together with an optimal divergence of both beams without affecting the efficiency of the optical parametric amplification.

The final efficient frequency conversion into the deep UV spectral range takes advantage of the fact, that the single-mode operation results in a 2.5 ns pulse duration of the OPO signal significantly shorter than the duration of the third harmonic being 8 ns. As only the later part of the third harmonic pulse is used for the amplification process in the OPA crystals, the untouched early part can be used by adding an easily realizable 4 ns delay line in the third harmonic beam path between the OPA and the final sum frequency generation. For the final sum frequency mixing process in a type I BBO crystal, the linear polarization of the amplified beam at 772 nm had to be rotated by 90 degrees.

After all optimizations, a pulse energy of 200 mJ of the third harmonic and about 1 mJ of the OPO signal are sufficient to produce up to 15 mJ of idler radiation from the OPA at 772 nm (and 17 mJ signal radiation at 657 nm) and finally 10 mJ of the UV radiation at 243 nm in 2.5 ns. In total this means 1% efficiency of the energy conversion from the fix-frequency near infrared radiation of the Nd:YAG laser into tunable UV radiation. Taking into account the reduction of pulse duration more than 3% conversion efficiency is achieved.

4.3 Measuring scheme at 243 nm

The pulse energy of the UV laser output is reduced to less than 1 mJ to produce enough signal without saturation. The beam is directed to the experiment using high-reflective dielectric mirrors with a high damage threshold. Acting as a beam splitter, a partially reflecting mirror divides the laser beam into two parts, which are directed counter propagating into the measuring cell. A delay line, Fig. 4.5, equalizes the path length of both beams. Another reason for introducing an additional reflection in the beam path is to provide a retro-reflection of the two counter propagating beams. This means that in the case of position fluctuation of the laser beam, both measuring beams are displaced in the same direction to maintain the overlapping condition in the measuring volume.

In order to reduce the beam size, the two counter propagating beams are slightly focused each with a lens of 500 mm focal length and a focus behind the measuring cell. This prevents hot spots and provides a better homogeneity of the intensity distribution of the two beams in the measuring volume. While tuning the frequency of the laser, the resonant two-photon absorption is detected as an optogalvanic signal, as described in Chapter 4.5.

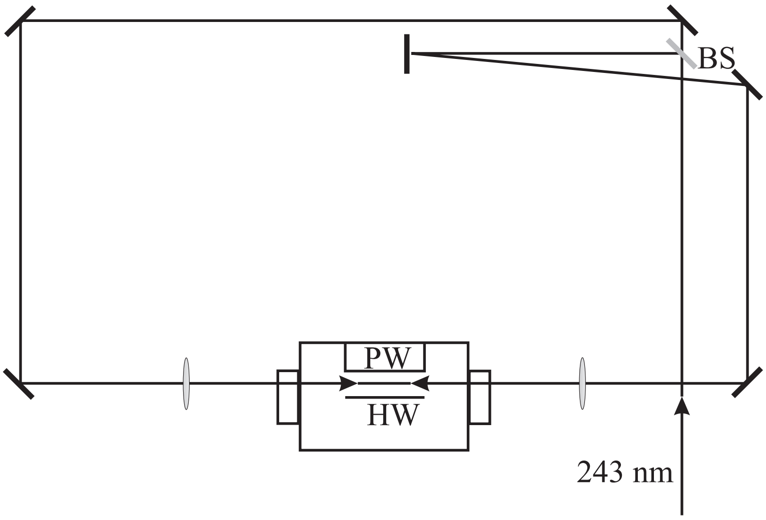

Figure 4.5: Optical scheme for two-photon excitation in a hydrogen cell, BS–beam splitter, HW–hot filament, PW–pick-up wire.

4.4 Laser system at 205 nm

As result of the experience in sensitive spectroscopic techniques and lasers suitable for plasma diagnostics, a pulsed laser system generating tunable, high power single-longitudinal-mode (SLM) UV radiation at wavelengths down to 200 nm was developed in our laboratory, as a Ph.D. work [1]. The system was specially optimized for the radiation at 205 nm which is required for the 1s-3s/d two-photon transition of atomic hydrogen.

The pulsed laser system is based on the same modular concept as the laser system at 243 nm [76] being able to solve the difficulties of tunable pulsed laser system in the UV wavelength range like for example SLM operation, good frequency control and high pulse peak power. Unlike the laser system at 243 nm which uses an improved commercial OPO with an intracavity grating, the 205 nm-laser system has an injection seeded OPO developed in our laboratory with special performances.

4.4.1 Optical parametric oscillator

The set-up of the OPO part of the laser system is shown in Fig. 4.6. The OPO consists of a nonlinear KTP crystal placed inside a short plane-parallel cavity, Fig. 4.7. The KTP crystal has been chosen because it has a high non-linear coefficient responsible for a high conversion efficiency, a narrow spectral acceptance favorable for SLM operation and a high damage threshold providing a safe operation. The material is also not hygroscopic. The crystal is 15 mm long with a quadratic cross section 7.5 mm × 7.5 mm. It was cut at 58.5° for type II phase matching. Its entrance and exit surface are covered with an anti-reflection coating: $R_{532nm} < 0.002$, $R_{710-910nm} < 0.03$, $R_{1.2-2.1\mu m} < 0.08$. To achieve the phase matching condition for a desired wavelength, the crystal is mounted on a rotary stage and depending on its angular orientation it splits the pump beam frequency ω_P into signal and idler frequency $\omega_P = \omega_S + \omega_I, \omega_S > \omega_I$. The plane resonator is resonant only for the signal wave at 820 nm and as short as possible to utilize a high OPO dynamics for reliable SLM operation. The distance between the mirrors is 18 mm and the optical length taking into account the refractive index of the crystal is 33 mm. Both mirrors are coated for a high transmission at the pump and the idler wavelengths ($T > 92\%$) and for a high reflectance at the signal wavelength with $R_{820nm} = 98\%$ for the input coupler and $R_{820nm} = 63\%$ for the output coupler.

The OPO is pumped single pass with 10% of the second harmonic (532 nm) of a 10 Hz Q-switched injection-seeded Nd:YAG laser (Continuum PL9010). The pulses have a Gaussian temporal profile with a pulse length of 8 ns (FWHM). A variable attenuator allows variation of the pump energy up to 30 mJ/pulse. A 2.5 times Galileo telescope makes a divergence control possible and compresses the beam to a final diameter of 1.2 mm (FWHM) with a maximum irradiance of 100 MW/cm^2 at the OPO crystal.

Single longitudinal mode operation with a high frequency control is provided by seeding the OPO with a cw external cavity diode laser (ECDL). The first diode laser had to be exchanged because of its bad tuning performance (mode hop) and low quality output characteristic. The new diode laser (New Focus, Vortex 6017) delivers a stable single-frequency output power of up to 10 mW and provides a tuning interval of 200 pm (90 GHz) around 820.5 nm. A two-stage Faraday isolator, producing no changes in polarization, protects the diode laser against back reflections from the OPO. Out-coupled from the Faraday isolator, the reflected beam is directed into a wavemeter for a wavelength control.

The pump and the seed beam overlap non-collinearly in the resonator. A horizontal angle between the beams compensates partly the walk-off of the signal beam [77] and allows an easier beam separation after the OPO with a Pellin-Broca prism. It is also necessary to introduce a small vertical angle between the beams to achieve a high output pointing stability, although it reduces the OPO efficiency to around 60%. SLM operation of the OPO is achieved when the cw seed laser frequency is in resonance with a cavity mode while the crystal orientation fulfills the phase-matching condition for the frequency splitting of the pump laser with the signal frequency corresponding

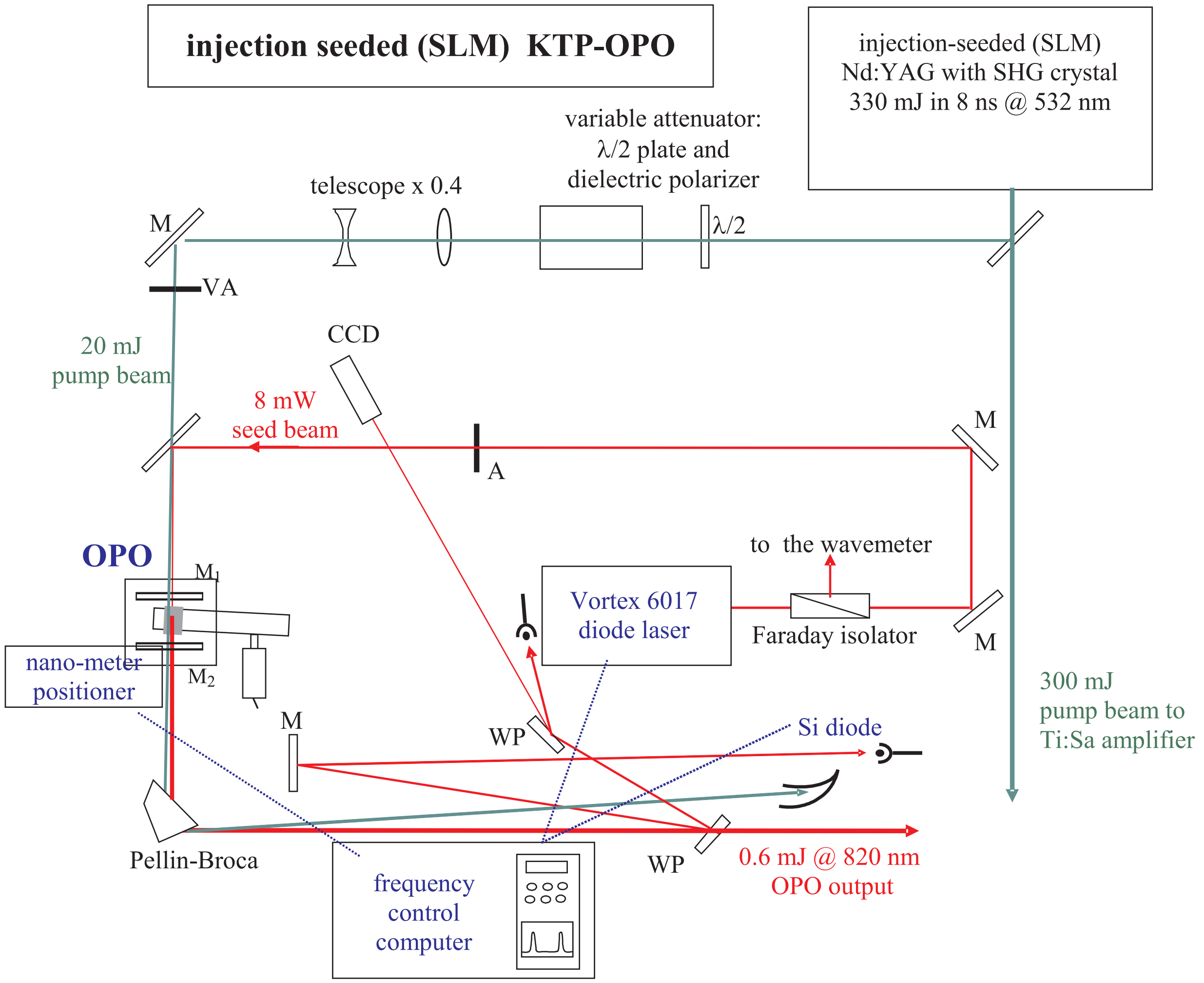

Figure 4.6: OPO set-up, M–mirror, M1–in-coupling and M2–out-coupling mirror of the OPO resonator, WP–wedge plate, A–aperture, VA–variable aperture.

to the seed laser frequency.

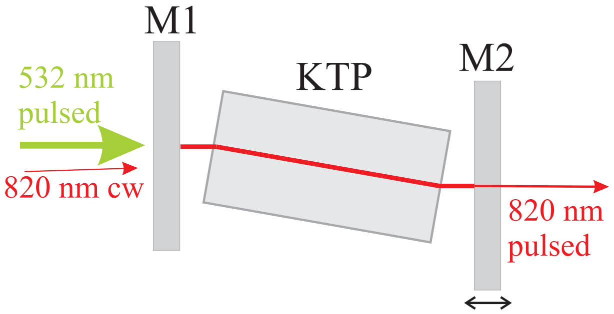

Figure 4.7: Seeded OPO resonator.

Although the commercial diode laser is tunable via a piezo control, the tuning of the pulsed OPO does not rely upon this control because piezo drives show a remarkable hysteresis and make a precise frequency tuning impossible. Instead, a novel concept has been applied for the OPO frequency control. It works in the following way. The output mirror of the OPO cavity is mounted on a linear positioning system with nanometer precision (Physik Instrumente GmbH&Co model P-750.20) which allows up to 75 μm linear and continuous movements with a resolution of 1 nm. Capacitive sensitive displacement detectors integrated in the positioning system allow a feedback and therefore high accuracy piezo movements. The feed forward is controlled through an external voltage supplied by a computer, making possible a total movement of 4.5 μm (50 GHz continuous scans) in 1 nm steps (10 MHz). The seed laser beam transmitted through the cavity is directed to a photodiode. The electric signal from the photodiode is recorded by computer and used to achieve mode matching. The seed frequency is locked on one side of the cavity transmission curve by the computer, applying an external voltage to the seed laser. The stabilization at 80% of the maximum transmission is suitable because the OPO efficiency is insignificantly changed and small variations of the transmission are easily observable, which is not the case in the maximum of the curve, Fig. 4.8. Besides the transmission of the seed laser, the photodiode detects also the 8 ns pulsed signal from the OPO output every 100 ms. During the pulse and a short waiting time after, the seed laser frequency remains constant. A short electrically saturated answer of the photodiode to the OPO pulse allows the frequency control during the time between the pulses.

Pumped with 20 mJ (about twice the value at threshold), the OPO signal output at 820 nm has reached 0.7 mJ pulse energy with a duration of 5.5 ns (FWHM) and a build up time of 2.5 ns. These values correspond to an

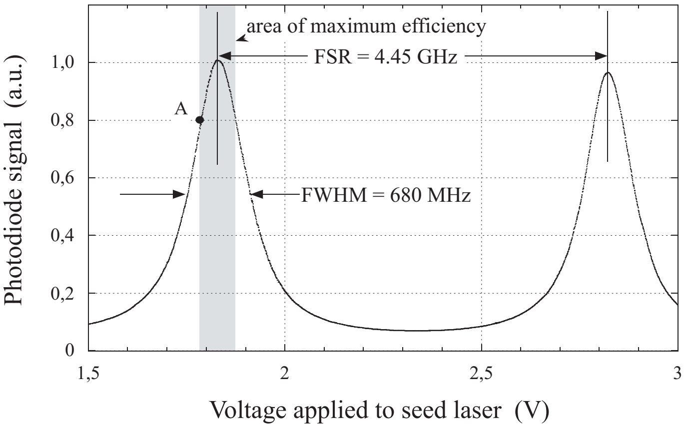

Figure 4.8: OPO cavity transmission curve measured with the cw-diode laser only, [1]. A is the stabilization point.

efficiency of 3.5% in energy and 5% in peak power. The efficiency could be increased with a higher pump power but this would degrade the spectral and spatial beam quality and the frequency control.

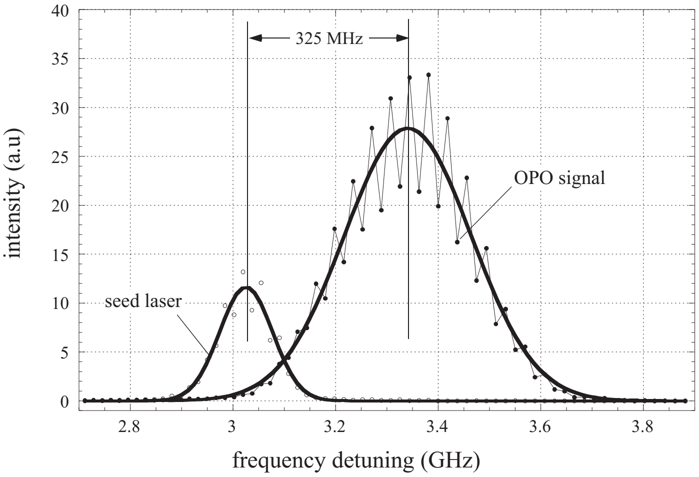

Figure 4.9: Frequency shift of the OPO signal from the seed laser measured by a Fabry-Perot interferometer, [1].

The spatial profile of the OPO signal is almost a Gaussian profile with a little bigger divergence in vertical direction remaining below 1 mrad. When the frequency is stabilized, the pulse to pulse energy fluctuations are below 5%, mainly due to the fluctuations of the pump beam. When the frequency is tuned, the fluctuations increased to 7.5% showing a small modulation as well.

A frequency analysis of the OPO signal shows good SLM operation with a spectral width of about 300 MHz, close to the Fourier transform limit of the pulses. The OPO output is frequency shifted from the seed laser by 325 MHz, Fig. 4.9. The 80% locking point has been chosen so that the pulsed OPO shifts towards maximal transmission. A frequency drift of about 1 GHz/h is present because of a small temperature change of the experiment table during operation.

4.4.2 Ti:sapphire amplifier

The pulsed OPO signal at 820 nm is amplified in a second part consisting of two Ti:sapphire crystals pumped by the remaining 300 mJ of the Nd:YAG second harmonic energy. The first crystal is pumped with about 100 mJ and the second one with 200 mJ. In addition to the new diode laser for seeding, the amplifying part was modified during this Ph.D. work from its first set-up. An optimized design was necessary to achieve an easier adjustment, better beam characteristics and an increase of the output energy.

To amplify the OPO signal from 0.6 mJ up to 50 mJ, the old set-up used a four pass amplification scheme with the same geometry in both crystals, Fig. 4.10. In the new set-up, Fig. 4.11 there is a six-pass amplification in the first Ti:sapphire crystal and a two pass amplification in the second crystal. The six-pass amplification in the first part is preferred for an optimal use of the pump beam power. To sustain a good beam profile, the pulse energy extracted from a Ti:sapphire crystal should not exceed 20% of the pump beam energy resulting in a single pass amplification up to 2 times in the first pass reduced in every next pass. With a low input energy and four passes only a small part of the pump energy could be used, while this amount is increased with six passes to almost the whole possible energy. At the same time a better starting condition with a higher input energy also improves the efficiency of the pump energy extraction in the second crystal. The amplification in the second part is less critical due to an increased diameter of the pump and the signal beam leading to a usage of a bigger crystal volume.

Although there are six passes in the first part, the geometry is much more compact in comparison to the previous one. As 90° turning mirrors in the new design, small prisms with a high reflecting coating at 820 nm/45° on the side of the hypotenuse are used, placed at a distance of about half a meter from the Ti:sapphire crystals. A single normal reflecting mirror is positioned directly behind the first crystal for all signal beam reflections at this side, see Fig. 4.11. At the same time this mirror is transparent for the pump beam passing from the back side. This set-up have shortened considerably the total path length of the beam in the amplifying part from 7.2 m to 4.8 m. The

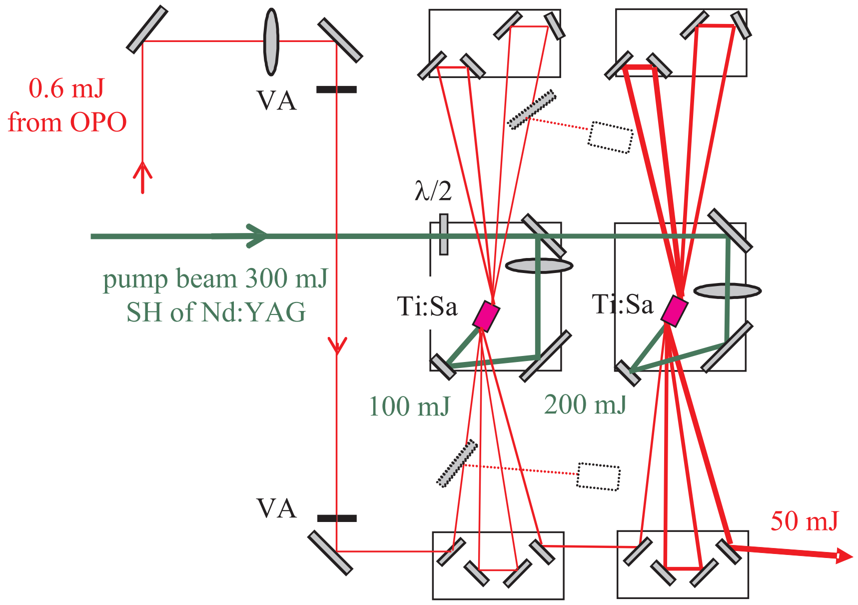

Figure 4.10: Old set-up of Ti:Sapphire amplifier.

improvement resulted in a significantly reduced increase of the beam's size due to its divergence, and a lens for the beam preparation in the amplifying part was no longer needed. On the other side the more compact geometry has brought less deviation from the optimal Brewster angle for the beams entering the Ti:sapphire crystals by reducing the maximum difference from 5.5° to 2.6° in the new set-up.

Before switching on the pump energy to the Ti:sapphire crystals, an optimal alignment and good beam profiles are achieved by adjusting the beam direction with the turning prisms and observing the beam profiles which are transmitted through the normal reflecting mirror on a CCD camera placed behind it.

This camera is also used to control the beam profile after the first crystal. The amplification in the second crystal is optimized simply by controlling the beam power.

In order to obtain p-polarization at Brewster angle for maximum absorption in the Ti:Sapphire crystal [78], the pump beam polarization is rotated with a half wave plate. The diameter of the pump beam within the crystal is adjusted by a convergent lens in both parts of the amplifier. This provides an optimal pumping, but prevents significant thermal lensing inside the crystals which could destroy the beam quality of the amplified beam. Due to the aging of the lamps pumping the Nd:YAG rods, the power and more importantly the divergence of its second harmonic are slowly changing and positions of the lenses have to be rearranged after some time to maintain optimal pump conditions of the amplifier crystals and especially in the OPO crystal.

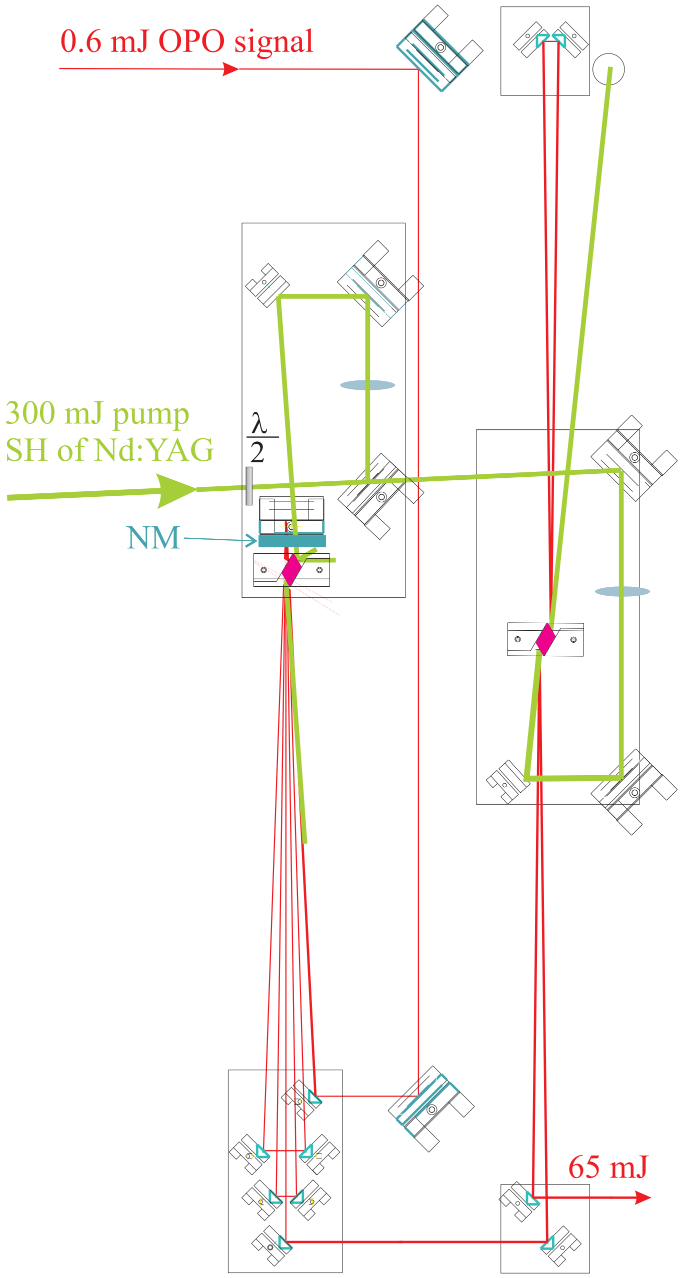

Figure 4.11: New set-up of the Ti:Sapphire amplifier. NM–normal reflecting mirror.

With all the modifications optimized in the new set-up of the Ti:Sapphire amplifier, 0.6 mJ pulse energy of the OPO signal output is routinely amplified to 14 mJ after the first crystal and finally to 65 mJ after the second crystal.

4.4.3 UV generation

UV radiation at 205 nm is obtained by stepwise sum frequency generation to the second, third and fourth harmonic of the amplifier output at 820 nm, see Fig. 4.12. For this harmonic generation three type I BBO crystals are used cut at 25.8°, 42.8° and 61.2°, each with an aperture of 8 mm × 8 mm and 7 mm long. BBO is a negative uniaxial nonlinear crystal with an optical transmission to below 200 nm, a large effective nonlinear coefficient, a high damage threshold and a low thermo-optic coefficient. To obtain a maximal conversion to the fourth harmonic three parameters have to be optimal: the polarization, the divergence and the irradiance.

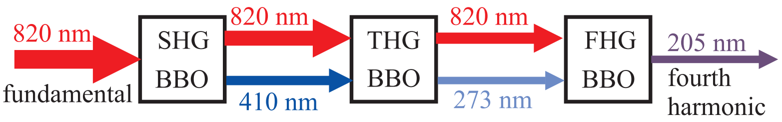

Figure 4.12: Chain of three sum frequency generation processes for the generation of UV radiation at 205 nm from 820 nm.

The polarization of the fundamental beam needed for the third harmonic generation is perpendicular to the polarization needed for the second and forth harmonic. Because of that reason the horizontal linear polarization of the fundamental beam is rotated with a half wave plate, before starting the harmonic generation process, Fig. 4.13. Such a polarization of the fundamental beam can be considered as the sum of a horizontal and a vertical polarized beams. In the first crystal, the horizontally polarized fundamental beam is partly converted to its second harmonic polarized in the vertical direction. The second harmonic and the vertically polarized part of the fundamental are added in the second crystal to the horizontally polarized third harmonic. This is finally summed with the leftover of the horizontally polarized fundamental in the third crystal giving the fourth harmonic polarized in the vertical direction. In this set-up, Fig. 4.13 a maximal conversion efficiency is obtained with the half wave plate rotated about 30°.

The next critical parameter is the beam divergence because of the limited acceptance angle of the BBO crystal, which decreases strongly towards smaller wavelengths, Table 4.1. On the other side after amplification in the Ti:sapphire crystals, the resulting high irradiance of the beam can cause a violation of the optimal phase matching in the central part of the BBO

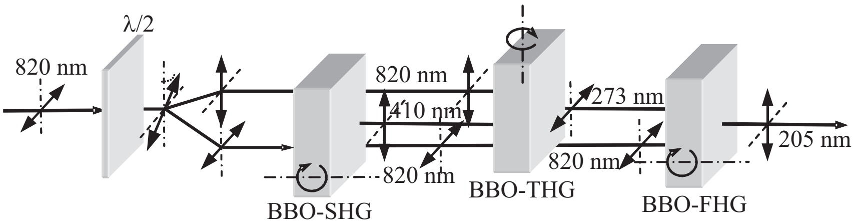

Figure 4.13: Fourth harmonic generation in three BBO crystals optimized with a half wave plate.

crystals due to induced thermal changes of the refractive index. The both tasks, the optimization of beam divergence and the necessary reduction of the irradiance, are solved by enlarging the beam diameter with 1:2 adjustable telescope. This provides a more homogeneous spatial distribution and a double sized beam, slightly smaller than the crystal aperture. Together with the possibility of small adjustments of the telescope, this preparation of the fundamental beam ensures a stationary condition and a high efficiency of the conversion processes.

process	SHG	THG	FHG
wavelength (nm)	820	410	273
acceptance angle (mrad· cm)	0.74	0.28	0.19

Table 4.1: Acceptance angle of a BBO crystal for second (SHG), third (THG) and fourth (FHG) harmonic generation.

The fourth harmonic beam is separated by six reflections of dielectric coated mirrors, which are high reflective at 205±5 nm and transparent at the wavelengths of the fundamental, second and third harmonic, see Fig. 4.14. The wavelength separation performed in this way provides a sufficient reduction of the unwanted wavelengths with minimal absorption losses at 205 nm.

The final output at 205 nm has about 5 mJ pulse energy in 4.5 ns (FWHM). This yields about 10% efficiency for the conversion of the fundamental beam with 60 mJ pulse energy in 5.5 ns.

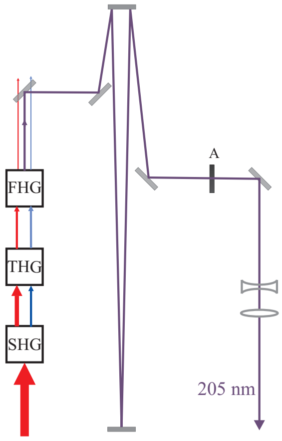

Figure 4.14: Separation of the fourth harmonic from the fundamental, second and third harmonic by six reflection of mirrors high reflective at 205±5 nm.

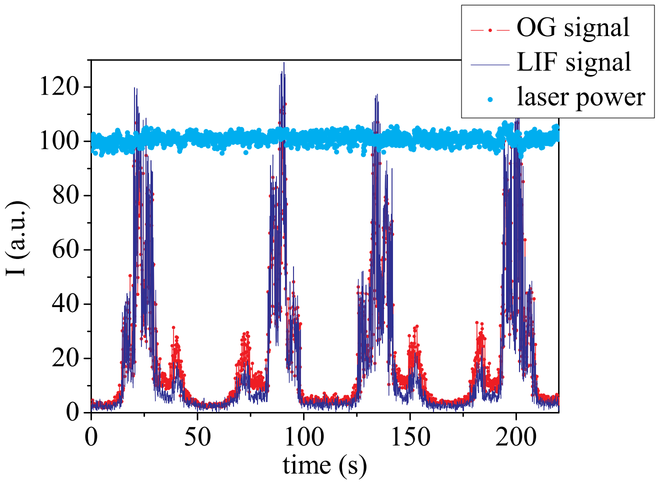

Figure 4.15: Power stability of the 205 nm laser beam measured with a UV sensitive photo diode during two laser scans in forward and backward direction across the hydrogen 1s-3s/d resonance.

The good performance of the OPO signal is maintained during the amplification and harmonic generation processes obtaining the UV radiation with a spectral bandwidth of about 300 MHz at 205 nm. In addition to the high pulse energy and the narrow bandwidth, the system provides a good pulse to pulse reproducibility and scan linearity very important for two-photon laser spectroscopy. An example of the laser power recording during a wavelength scan two times in forward and backward direction across the resonance of the hydrogen 1s-3s/d transition is shown in Fig. 4.15.

The UV beam is directed through controlling apertures and enlarged with a Galileo telescope to improve the beam homogeneity and to prevent "hot spots" in the further beam propagation, Fig. 4.14.

4.5 Measuring scheme at 205 nm

Only a moderate pulse energy of 1.5 mJ is used for the measurements. The 205 nm laser beam is divided by a beam splitter and the two beams are directed counter-propagating into the measuring cell as shown in Fig. 4.16, obeying all the rules mentioned in Chapter 4.3. Both beams are focused with 1 m lenses, and the measurement volume is about 20 cm before the foci of both beams. In the center of the measurement volume the beam diameters are 1 mm resulting in a laser irradiance of about 50 MW/cm^2, which is sufficient for the two-photon excitation of hydrogen atoms, but does not cause a significant power broadening or a dominant photo-ionization.

The measurements with optogalvanic (OG) and fluorescence (LIF) detection were performed simultaneously for three different cases of the laser polarization, namely both laser beams linearly polarized parallel to the electric field (p-polarization), perpendicular to the electric field (s-polarization), or circularly polarized exciting $\Delta m = 0$ transitions. The laser beam is originally polarized linearly in the vertical direction, parallel to the electric field. For the other kind of measurements, the polarization is varied introducing half wave or quarter wave plates in both counter-propagating laser beams.

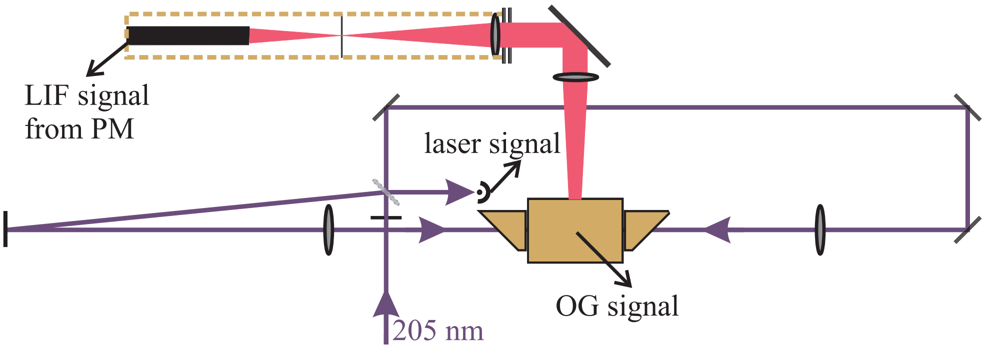

Figure 4.16: Scheme of the measurements with the 205 nm laser beam. Simultaneous detection of the LIF and the OG signal and the laser pulse energy is denoted.

The charged particles produced by two-photon excitation and subsequent ionization by the absorption of a third laser photon are accelerated in the applied electric field. The ion current collected by the pick-up wire is measured as a voltage pulse across a variable resistor (Fig. 4.1) giving the possibility for signal intensity and duration variation to achieve an optimal signal level for different conditions. Otherwise the OG signal is easily saturated in high electric fields or the signals are very weak in low fields. A minimal electric field of about 10 V/cm is necessary to accelerate the ions towards the pick-up wire and make OG detection possible. The OG signal is amplified, A/D converted and recorded by a computer.

The Balmer-alpha fluorescence radiation at 656.3 nm, emitted from the two-photon excited hydrogen atoms, is collected perpendicular to the direction of the laser beams with a lens placed at a distance of its focal length $f = 250$ mm from the laser beams. The parallel propagating radiation is then directed with a turning mirror into a light sealed detecting pipe. At the entrance of the pipe there are two interference filters with a central transmission wavelength at $\lambda = 656$ nm and bandwidths (FWHM) of $\Delta\lambda = 10$ nm and $\Delta\lambda = 5$ nm. The filtered radiation in the pipe is refocused with a second lens of the same focal length $f = 250$ mm. In the image plane of the measurement volume at the focal position of the second lens, there is a slit aperture which acts as spatial filter to suppress remaining stray light and to improve the spatial resolution of the LIF measurements. The volume where the measurements are performed is defined by the 30 mm long hot filament producing hydrogen atoms and the diameter of the overlap region of the laser beams equal to 1 mm where hydrogen atoms are excited. In the case of the OG detection charged particles are collected from the whole volume by the pick-up wire which has the same length as the filament. In the LIF measurements, however, this volume is imaged 1:1 in the focal plane of the second lens. The slit size of 0.3 mm × 20 mm is remarkable smaller then the excitation volume of hydrogen atoms, which improves the spatial resolution of the measurements. At the same time the region where end effects of the wires are present is blanked off. The divergent radiation behind the slit aperture is collected by a photomultiplier (Electron Tubes 9129B) at a distance of 150 mm where the size of the fluorescent light beam has enlarged to the 30 mm size of the photocathode. That way the whole photocathode area is illuminated uniformly which prevents a saturation or a damage of the photocathode surface by the intense Balmer-alpha photon pulses only slightly longer in time then the laser pulses. Together with the linear focused dynodes of the multiplier and a voltage divider designed for good linearity in pulsed applications this provides a photomultiplier with an optimal performance. At an applied voltage of 1.6 kV its nominal gain is 10^6 and its response time for a single electron is 3.5 ns (FWHM). The amplified charge pulse with a nanosecond pulse duration is transferred to a preamplifier (ORTEC 113 scintillation preamplifier) and integrated with a 1 nF capacitor with an electrical fall time of 50 μs. The dc part of the input signal of the preamplifier is separated and measured independently with a sensitive amperemeter. This provides a control of the unblocked part of the dc background light coming from the filament heated to incandescence. For example the tungsten filament at a current of 90 A and the photomultiplier operated at 1.6 kV resulted in a dc current of 0.2 μA. The pulsed preamplifier output is coupled to a pulse shaping amplifier (ORTEC 673 Spectroscopy amplifier) with pole-zero cancelation for reduction of the undershoot caused by the exponential tail of the preamplifier signal, with a shaping time constant set to 6 μs and a gain factor set to 100.

The laser pulse energy at 205 nm is measured with an UV sensitive photodiode. The amplified signal from this photodiode and the amplified OG and LIF signals are measured simultaneously for every laser pulse. The A/D conversion of these three signals is performed by a multi-function I/O board (National Instruments NB-MIO-16). Four input channels are activated for an external-triggered operation of the input multiplexer. The subsequent A/D conversion (12 bit resolution every 10 μs) of one input signal after the other is synchronized by an external trigger. This trigger is provided by a home made delay box where four trigger pulses with 10 μs time separation are produced from the Nd:YAG laser Q-switch trigger signal. The delay between the laser pulse and the first conversion trigger is adjusted to digitize the maximum of the LIF signal pulse entering the first input channel. The second and the fourth channel input is used to measure the OG signal at an early and a 20 μs later time so that the difference allows to filter out small signals. When the early signal is in saturation only the later signal is used. The third input channel represents the laser pulse energy. The four digitized signals are recorded by a computer at the 10 Hz repetition rate of the laser.

Chapter 5

Results and discussion

5.1 Measurements at 243 nm

5.1.1 Doppler broadened background

As already mentioned, 243 nm laser radiation is applied for the 1s-2s excitation of atomic hydrogen. Two counter-propagating laser beams with linear polarization and equal intensity are used to obtain a Doppler-free excitation. Nevertheless by observing the OG spectrum on a scan interval much larger than the narrow Doppler-free resonance, one can notice an extended Doppler-broadened background as shown in Fig. 5.1. This background (green part of the spectrum) originates from the absorption of two photons from the same laser beam, a process with half the probability of the two-photon absorption from each of the two beams. The second process gives the characteristic Doppler-free spectrum (red part of the spectrum) on the top of a broad Doppler-profile.

Showing a Doppler broadening, which far exceeds the fine structure of the hydrogen $n = 2$ level the spectrum in Fig. 5.1is a nice example for the necessity of a Doppler-free spectrum for the measurement of electric fields. At the same time the Doppler background opens the possibility to estimate the kinetic temperature of the hydrogen atoms under the measuring conditions. The Doppler broadened part is fitted with a Gaussian profile not taking into account the Doppler-free part, Fig. 5.2. A spectral width (FWHM) of 20 GHz is obtained (at the laser wavelength). Application of the formula for the Doppler broadening:

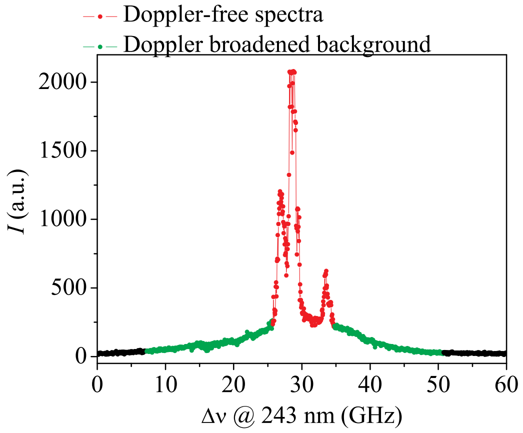

Figure 5.1: Doppler-free spectra on the top of a Doppler-broadened background by two-photon excitation of atomic hydrogen at 243 nm.

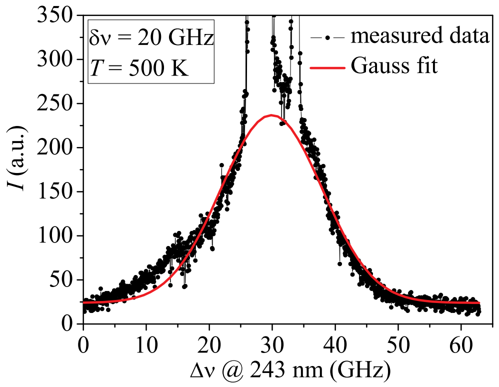

Figure 5.2: Doppler-broadened background fitted with Gaussian profile.

$$\delta_\nu = 7.162 \cdot 10^{-7} \cdot \nu \cdot \sqrt{\frac{T}{M}} \tag{5.1}$$

where δ_ν is the FWHM of the Gaussian profile, ν the transition frequency (the same unit as the measured FWHM, in our case calculated at the laser wavelength), M is the relative atomic mass being 1 for hydrogen, results in a kinetic temperature T of 500 K for the hydrogen atoms in the measurement volume.

5.1.2 Hydrogen spectra

In the following, only the Doppler-free part of the spectrum is discussed, because the highly resolved components are important for the measurements of electric fields.

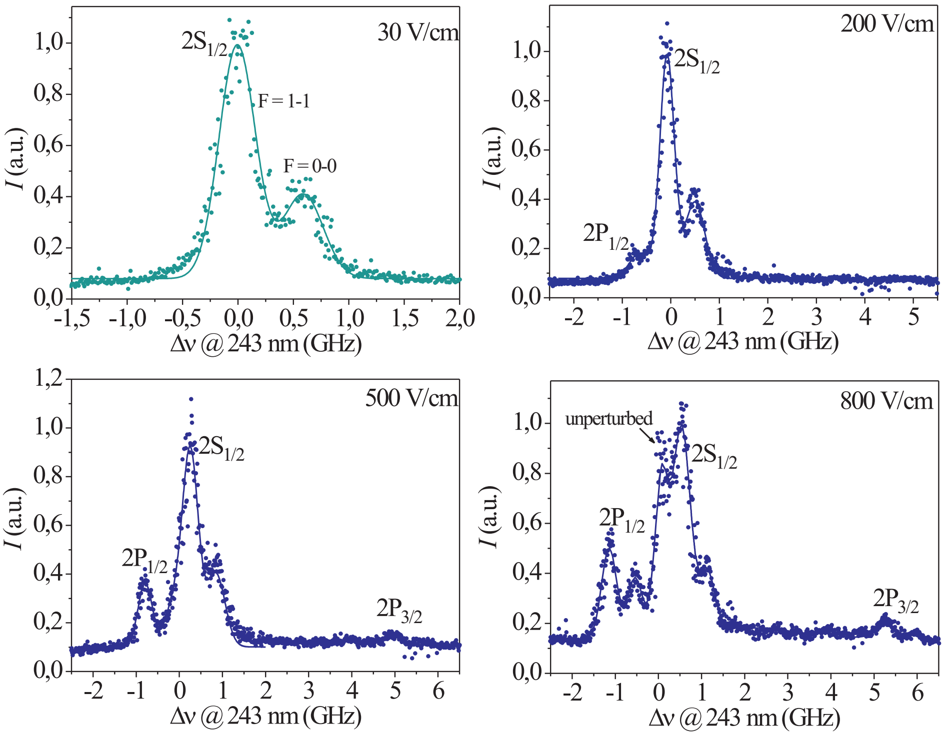

Figure 5.3: Spectra of the two-photon excited $n = 2$ level of hydrogen for different electric field strengths.

Examples of recorded spectra with two photon excitation at 243 nm and OG detection for different electric field strengths are presented in Fig. 5.3. As already mentioned the selection rule for a two-photon absorption allows only transitions with $\Delta l = 0$, while $\Delta l = 2$ is not possible for the $n = 2$ level. If there is no external electric field interfering with the atom, two photons at 243 nm can excite hydrogen from the 1s ground level only to the 2s but not to any 2p level. The Stark effect changes this condition. In very low electric fields, shown in the first spectrum, only the allowed $2S_{1/2}$ component is present. The two hyperfine components $F = 1$ and $F = 0$ are resolved, dominated by the ground state with the largest splitting influencing the hyperfine structure. The fine structure components of the $n = 2$ level show much smaller hyperfine splitting, see Chapter 2.1.3 and Table 2.1.[1] The two hyperfine components always consist of a strong and a weak part with an intensity ratio 3:1. This behavior is clearly resolved in the measured spectra because the hyperfine splitting is larger then the laser bandwidth of 300 MHz.

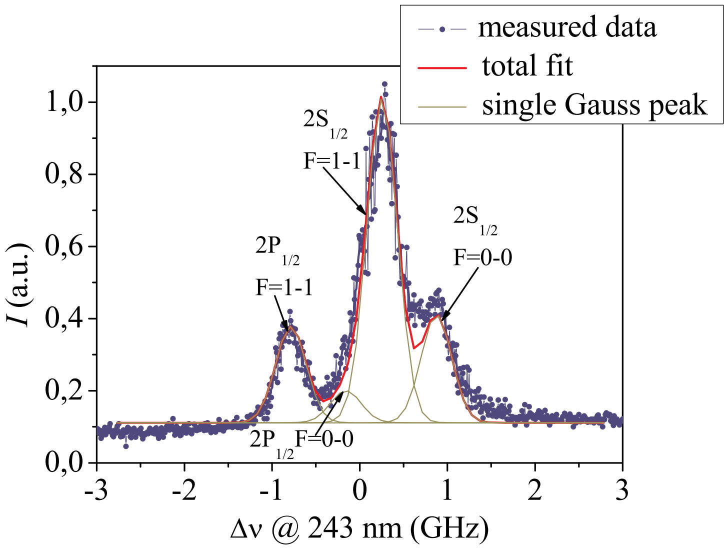

Figure 5.4: Example of a spectrum with all hyperfine components fitted with Gaussian profiles of the same width.

In the spectra of Fig. 5.3 one can see the stronger hyperfine component of the $2P_{1/2}$ appearing in higher electric fields. As the field increases, the separation between $2S_{1/2}$ and $2P_{1/2}$ increases and the weaker hyperfine component of $2P_{1/2}$ begins to separate from $2S_{1/2}$. In strong fields, the $2P_{3/2}$ component with its hyperfine structure is also observable in the spectrum. The presence of an additional unperturbed $2S_{1/2}$ component in strong electric field indicates that part of the hydrogen atoms is out of the influence of the electric field or in the areas with very low fields. The frequency separation of the forbidden $2P_{1/2}$ to the allowed $2S_{1/2}$ component is a direct measure of the perturbation by the external electric field.

In order to compare the measured frequency shift between the $2S_{1/2}$ and

---

[1] Here it should be pointed out that hyperfine splitting values in the Chapter 2.1.3 are given for the atomic resonances, while all the frequency values of the presented results as well as the laser bandwidth are at the frequency scale of the laser, which corresponds to half the value of the resonance frequencies (e.g. the hyperfine splitting of the ground state of hydrogen of 1420 MHz is equal to 710 MHz at the laser wavelength).

the $2P_{1/2}$ component with calculated values, the spectra have been processed in the following way: each component has been fitted with a Gaussian profile. Even if the weaker hyperfine components are unresolved, they have been taken into account with a 1:3 intensity ratio and a fixed frequency shift to the corresponding strong component. One example of a fitted spectra is presented in Fig. 5.4. All components have the same spectral width. The resulting FWHM of 400 MHz is slightly broader than the laser bandwidth, which is probably introduced by some inhomogeneity of the electric field. The positions of the stronger hyperfine components have been used for comparison with the theoretical results.

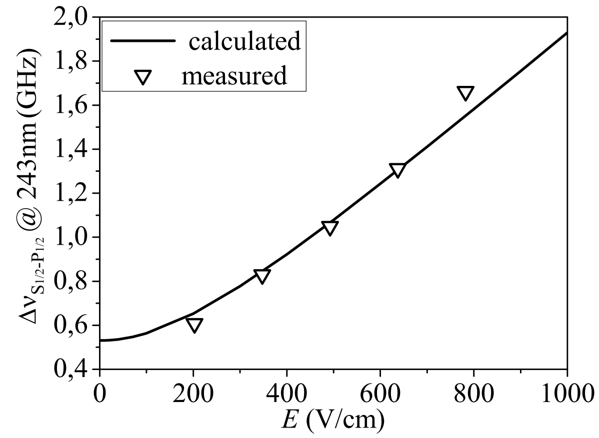

Figure 5.5: Measured and calculated frequency shift between the $2S_{1/2}$ and the $2P_{1/2}$ component of hydrogen vs. the electric field strength.

The frequency shift between $2S_{1/2}$ and $2P_{1/2}$ for different values of the electric field is shown in Fig. 5.5. The triangles indicate the measured points extracted from the experimental data and the solid line is the calculated curve. The uncertainty introduced by the laser bandwidth and by the determination of the position of components in spectrum is about 10%. The good agreement between the measured and the calculated values implies that the Stark shift between the $2S_{1/2}$ and the $2P_{1/2}$ is a reliable measure for electric field strengths down to 200 V/cm in plasma sources where the OG detection can be used.

5.1.3 Deuterium spectra

The same kind of measurements have been performed using deuterium instead of hydrogen. Due to the isotope shift (Chapter 2.1) the laser wavelength has to be changed from the central wavelength at 243.135 nm for hydrogen to 243.069 nm for deuterium. This change of 335 GHz at the laser wavelength, is significantly larger than the fine structure of about 6 GHz.

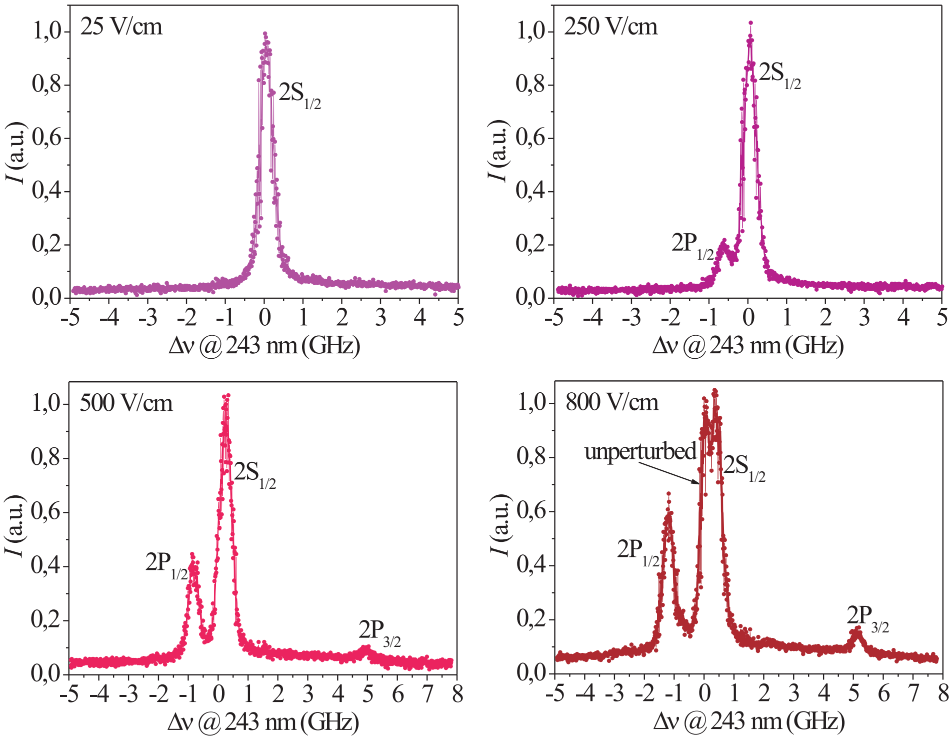

Figure 5.6: Spectra of the two-photon excited $n = 2$ level of deuterium for different electric field values.

The spectra obtained in deuterium for different electric field values are shown in Fig. 5.6. Compared with hydrogen, the hyperfine splitting of deuterium is much smaller, see Chapter 2.1.3. For that reason the hyperfine components are not resolved in the deuterium spectra. In low electric fields only the $2S_{1/2}$ component is present. With increasing field strength, first, the $2P_{1/2}$ component appears and with higher fields the $2P_{3/2}$ component as well. The absence of the hyperfine structure in the measured Doppler-free spectra can be considered as an advantage, because this results in simple and clear spectra with an easily noticeable influence of the electric field on the frequency shift and the intensity ratio of the only three fine-structure components, see Fig. 5.7.

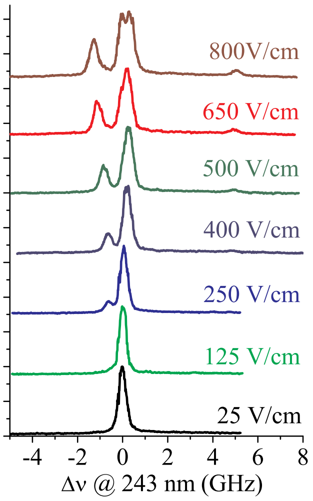

Figure 5.7: Influence of the electric field on the 1s-2s spectra of deuterium.

As in the case of hydrogen, the frequency shift between the $2S_{1/2}$ and the $2P_{1/2}$ component has been used for determination of the electric fields.

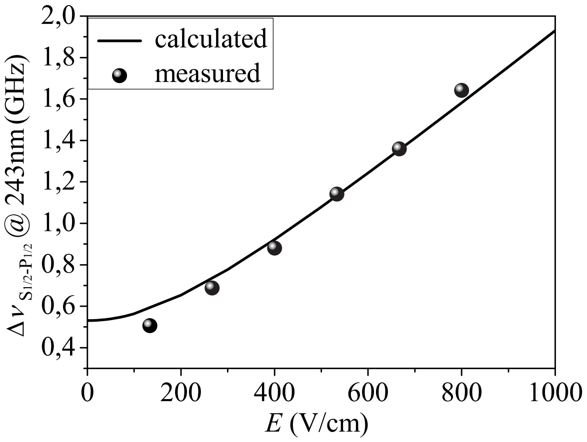

Figure 5.8: Measured and calculated frequency shift between the $2S_{1/2}$ and the $2P_{1/2}$ component of deuterium vs. electric field strength.

The calculated values of the frequency shift are the same because the

Stark splitting of all hydrogen isotopes is identical relative to the structures at zero-field. The spectra of different isotopes are clearly displaced by different resonance frequencies due to the relative large isotope shift [58]. As seen in Fig. 5.8 the measured Stark shift is consistent with calculated values for different electric field strengths, indicating the validity of this method for the measurements of deuterium. The low field limit is again about 200 V/cm.

5.2 Measurements at 205 nm

Excitation of the $n = 3$ level with tunable pulsed UV radiation has been used for measurements more sensitive to the electric field (below 200 V/cm) combined with the possibility of using fluorescence detection (LIF) in the visible range. The first test measurements were performed with OG detection only. As indicated by dotted lines in Fig. 5.9, the spectra with a clear influence of the electric field on the frequency shift between $3S_{1/2}$ and $3P_{1/2}$ increasing to nearly six times the Lamb shift value at 200 V/cm encouraged us to continue these measurements including LIF detection.

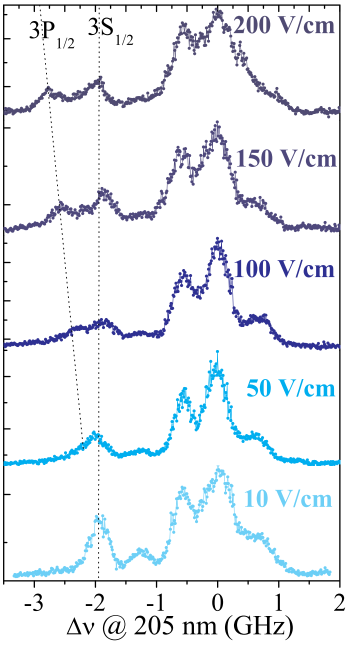

Figure 5.9: The first measurements of the two-photon excited $n = 3$ level of hydrogen with OG detection for different electric field strengths.

The final measured spectra with both OG and LIF detection for the three cases of laser polarization and different electric field values are presented in Figures 5.10, 5.11 and 5.12. The properties of these different two-photon absorption profiles are discussed in detail below .

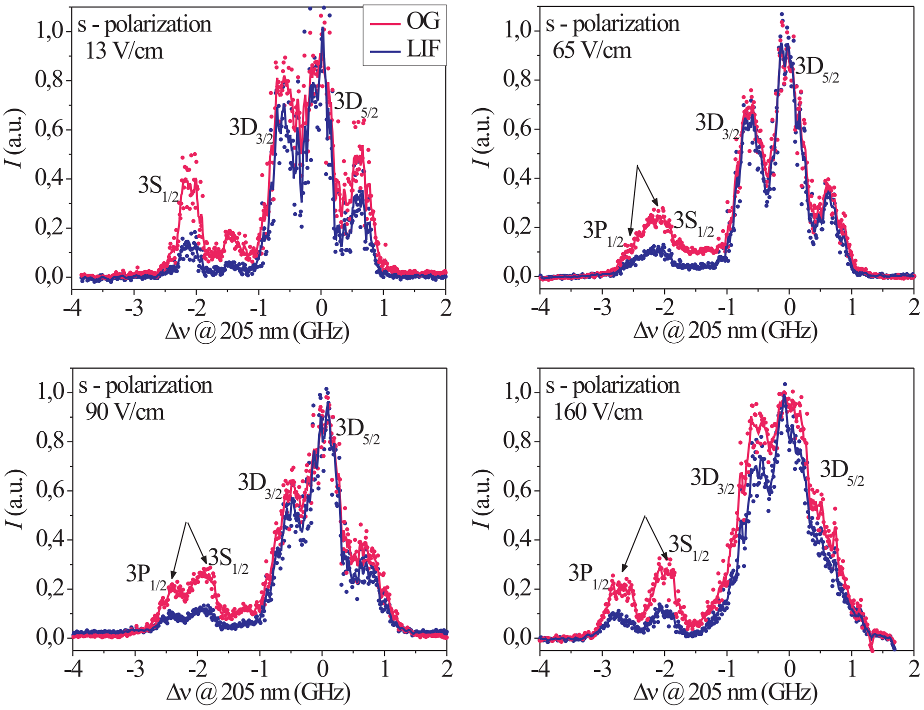

Figure 5.10: OG and LIF spectra of the two-photon excited $n = 3$ level of hydrogen for different electric field strengths. The two laser beams are linearly polarized perpendicular to the electric field, s-polarization. Arrows indicate the shift between the two components ($3S_{1/2}$ and $3P_{1/2}$) suitable for the field measurement.

The field-free spectra are not shown because in that case only LIF measurements are possible, while the detection of the OG signal requires a certain minimal electric field for the acceleration of the charged particles to be collected by the pick-up wire, Chapter 4. In weak electric fields with a field strength well below 50 V/cm, the two-photon transition to the $3P_{1/2}$ level remains forbidden due to the selection rules of the angular momentum. Therefore the spectra consist of s and d components only. The weak component on the low-frequency side corresponds to the $3S_{1/2}$ and the stronger components correspond to the $3D_{3/2}$ and $3D_{5/2}$ fine structure sub-levels of the $n = 3$ level. With an intensity ratio 3:1 the hyperfine structure introduces an additional weak component on the high-frequency side of each of these three components. This hyperfine structure is only caused by the hyperfine splitting of the $1S_{1/2}$ ground level while the hyperfine splitting of the $n = 3$ level components is negligible, see Table 2.1. In the spectra only five components are visible because the weak hyperfine component of $3D_{3/2}$ is hidden under the strong $3D_{5/2}$ component.

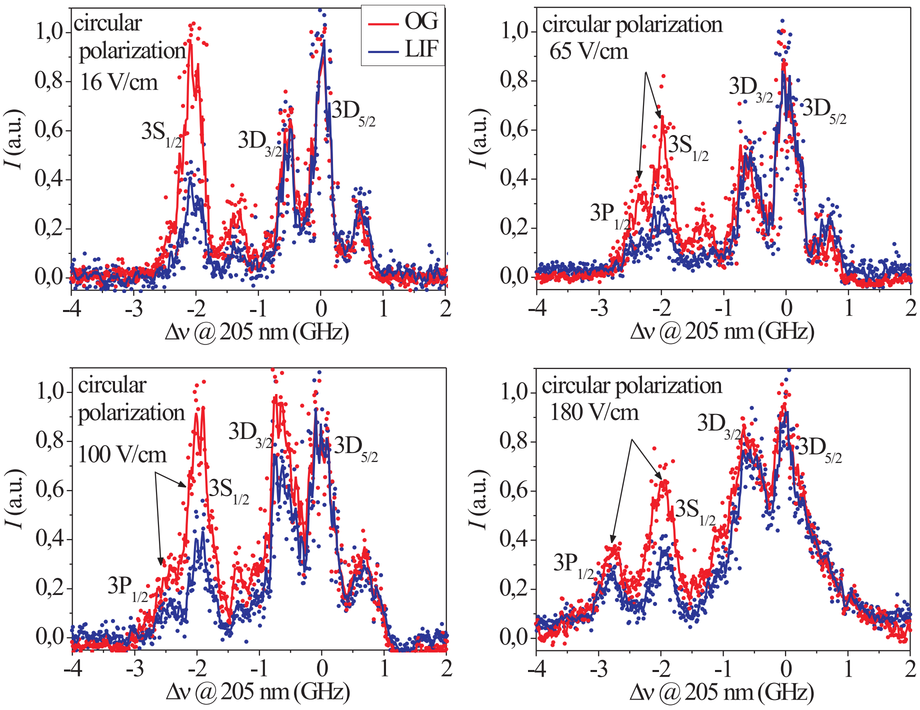

Figure 5.11: OG and LIF spectra of the two-photon excited $n = 3$ level of hydrogen for different electric field strengths. The two laser beams are circularly polarized exciting $\Delta m = 0$ transitions. Arrows indicate the shift between the two components ($3S_{1/2}$ and $3P_{1/2}$) suitable for the field measurement.

In the field-free case, the spectra should be identical for p- and s-polarization. Accordingly, the small difference of the OG spectra for the lowest measured field is caused by slightly different experimental conditions and the fact that only a part of the produced ions is collected by the pick-up wire in such a low fields. Due to the two-photon selection rules in the case of $\Delta m = 0$ circular laser polarization, the $3S_{1/2}$ component is much stronger in comparison with the d components. The $3S_{1/2}$ component in the OG spectrum is always stronger than in the LIF spectrum (with the d components normalized to the same intensity). This is attributed to the different transition probabilities for the processes following the two-photon absorption. Namely, the radiative transition probability from 3s to 2p is ten times smaller then the radiative transition probability from 3d to 2p [72]. These different Balmer-alpha emission probabilities influence the LIF signal but not the OG signal because the ionization probability is not much influenced by the levels' substructure [75]. Therefore the ratios of the components in the OG spectrum at low electric fields reflect the different two-photon absorption probabilities.

Concerning the comparison between the OG and the LIF spectra, it should be pointed out that the optogalvanic detection has a higher sensitivity i.e. a better signal to noise ratio. On the other hand, as explained in Chapter 4.5, fluorescence detection provides a higher spatial resolution. Nevertheless the OG spectra are not significantly broader then the LIF spectra as experienced from a similar comparison [41] regardless of possible electric field inhomogeneities.

In the presence of an electric field the forbidden $3P_{1/2}$ component appears on the low-frequency side of the $3S_{1/2}$ component. The $3P_{1/2}$ component grows with the field and its separation from $3S_{1/2}$ increases from the Lamb shift value at very low fields. As in the case of the 1s-2s excitation, the frequency shift between these two components is a suitable measure for the electric field strength because they remain always separated from other components. The lower field detection limit is reached when the $3P_{1/2}$ component is just distinguishable from the $3S_{1/2}$ component; hence the laser bandwidth plays a key role. This method of field detection can be used in the cases of s- and circular laser polarization, but not in the case of p-polarization where the $3P_{1/2}$ component is not visible in the spectrum. According to theory it just appears in weak electric fields with very low intensity, i.e. the $3P_{1/2}$ excitation probability remains less than the 1/10 of the $3S_{1/2}$ probability until a field strength of 500 V/cm.

On the other hand in electric fields grater than 100 V/cm, the strong central Stark components, originating from the splitting and mixing of the manifold of the $3D_{5/2}$, $3D_{3/2}$ and $3P_{3/2}$ components are smeared out in the cases of circular and s-polarization. However, this situation differs in the case of p-polarization with only two distinct central Stark components for higher fields. The frequency shift between these two individual components increases with the field strength and provides a good measure of electric fields. In Fig. 5.12 for electric field value of 200 V/cm we can even resolve the weak hyperfine $3D_{3/2}$ component between the two shifted strong components. Although both components remain allowed also at zero field, the weak dependence of the frequency shift on small electric fields sets a practical field detection limit similar to the limit in the other polarization cases.

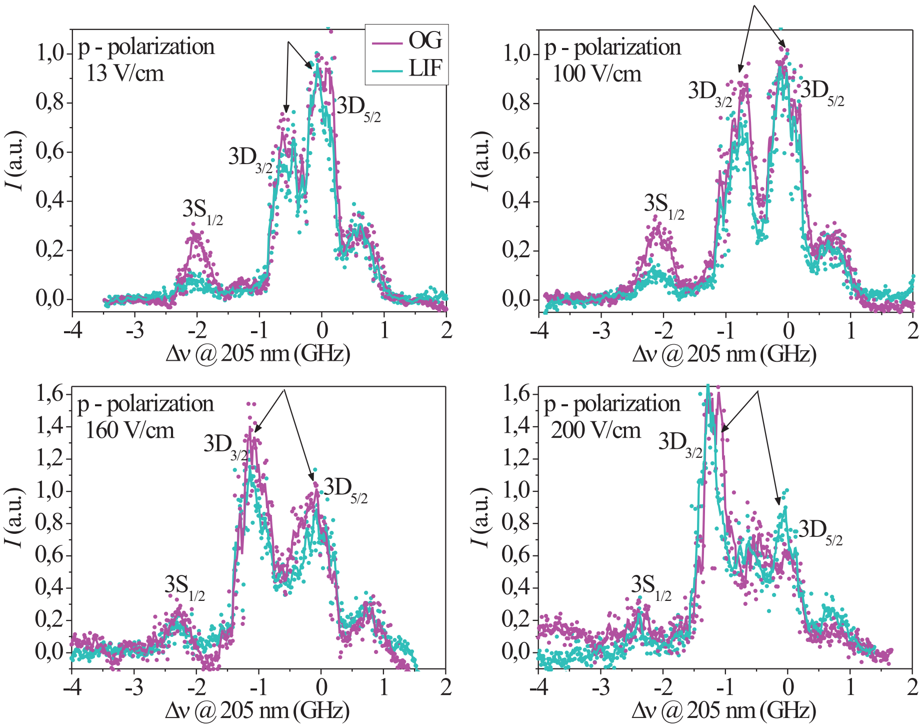

Figure 5.12: OG and LIF spectra of the two-photon excited $n = 3$ level of hydrogen for different electric field strengths. The two laser beams are linearly polarized parallel to the electric field, p-polarization. Arrows indicate the shift between the two components ($3D_{3/2}$ and $3D_{5/2}$) suitable for the field measurement.

Concerning the intensity of the spectral lines, one can notice from the spectra that the ratio of the forbidden $3P_{1/2}$ to the allowed $3S_{1/2}$ as well as the ratio of the $3D_{3/2}$ to the $3D_{5/2}$ component in the case of p-polarization depend on the electric field strength. But this quantity is not favorable to be used for field determination because it can not be easily calculated due to many influencing effects. Besides the two-photon absorption, one has to take into account the fluorescence yield and possible quenching collisions influencing the population of the excited state. These collisions depend on the discharge conditions, strongly varying from case to case. For that reason, even a calibration of the intensities' dependence upon the electric field strengths would not solve the problem in many cases.

For data evaluation, exact frequency positions in the spectra are obtained by fitting the interesting components including their hyperfine structure, all

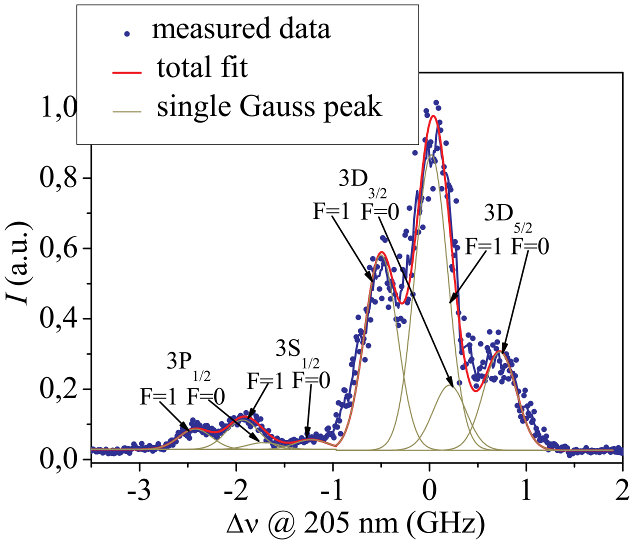

Figure 5.13: Example of spectrum with components fitted with Gaussian profiles. $F = 0$ or 1 indicates the ground hyperfine level of each component.

with Gaussian profiles of the same spectral width. As in the case of the 1s-2s excitation, the weak hyperfine components are included, even when being unresolved, with a 1:3 intensity ratio and with a fixed frequency shift of 710 MHz relative to the strong component. As example, a spectrum with fitted Gauss peaks is shown in Fig. 5.13. The spectral resolution expressed by the FWHM results to 400 MHz. The frequency positions of the strong hyperfine components are used for the comparison with the calculated results.

The resulting frequency shift dependencies on the electric field are presented in Fig. 5.14 for the three cases of different polarization of the laser beams. The solid lines are the calculated field dependencies, the dots are the data extracted from the measured spectra. The solid diamonds represent the LIF data and the empty circles the OG data. There is no significant difference between the results obtained from the two detection methods. One can notice that the deviation from the calculated curve is correlated with the relative discrepancy of OG and LIF data. This discrepancy is a measure of the uncertainty of the experiment and the data processing, caused by the field inhomogeneity in an unequal measurement volume for the OG and the LIF detection or by the variation of the laser output and the measurement conditions. The resulting relative uncertainty is varying from 8% for medium field values to 20% in low fields where the components are hardly resolved

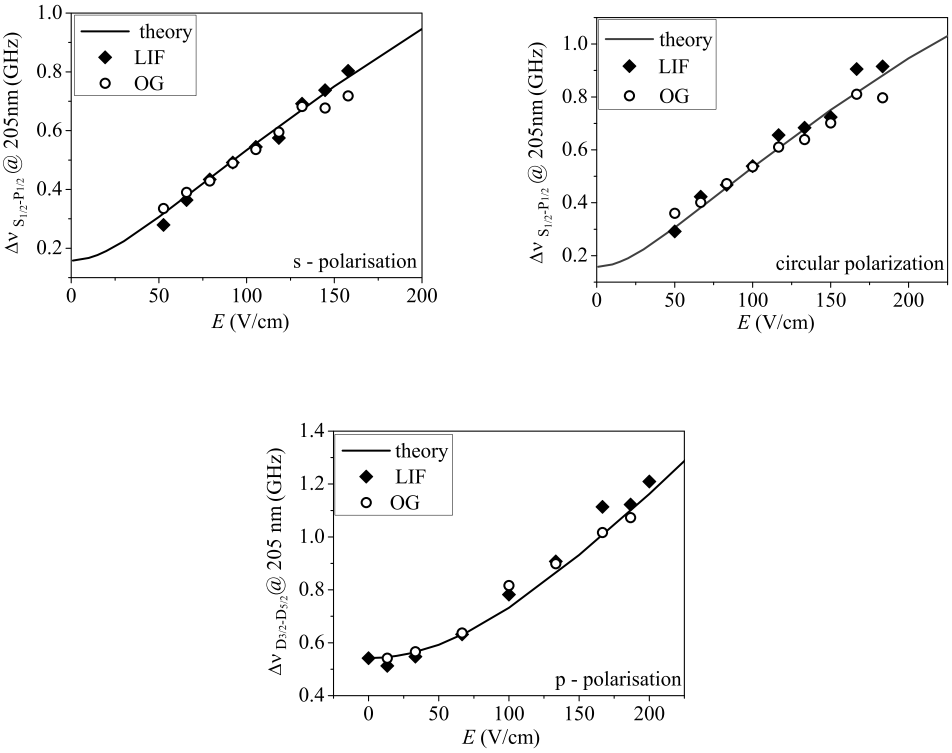

Figure 5.14: Measured and calculated frequency shift between the two components of hydrogen 1s-3s/d spectrum suitable for electric field measurements for different electric field strengths in three cases of laser polarization.

and 15% in the highest measured fields where the components are broadened due to the field inhomogeneity. In the case of circular polarization additional noise is introduced by the beams reflected from the windows in the measuring cell, mounted at 1° angle and not at the favorable Brewster angle as in the case of linear polarization. Nevertheless all three polarizations and both detecting methods yield a good correspondence of calculated and experimental results. Therefore in any case, the frequency shift of the selected line pairs is a suitable measure for the electric field strength. The consistent results indicate a promising further use of this method for the measurements of electric fields. With a single pulsed tunable UV-laser appropriate for high resolving Doppler-free spectroscopy of atomic hydrogen, electric fields of 50 V/cm or more can be measured.

Chapter 6

Conclusion

In this Ph.D. work the possibilities and the limitations of a simple, sensitive optical method for local electric field measurement in plasmas containing hydrogen atoms are explored. The method employs only a single excitation step, accomplished by Doppler-free two-photon absorption of laser radiation by ground-state atoms, and direct observation of the Stark splitting of the hydrogen level excited in this way.

The measurements represent a demanding performance test of the solid state laser systems used and of the modifications made for optimization. For the both pulsed single-longitudinal mode lasers used, tunable at 243 nm and at 205 nm, respectively, the measured spectra highlight that the achieved pulse to pulse reproducibility, narrow bandwidth close to the Fourier limit and the spectral stability during wavelength tuning are clearly sufficient to make the systems suitable for more wide use in high precision non-linear laser spectroscopy. The 243 nm laser has already been applied before for two-photon spectroscopy [79], while the 205 nm system, built up in a previous Ph.D. work [1], first had to be improved within this Ph.D. work as described above before it could be applied for precise measurements of Stark spectra in order to determine low local electric fields.

Hydrogen atoms are produced in a special low pressure cell by thermal dissociation at the hot surface of a tungsten filament. The electric field is controlled by the applied voltage between the filament and another wire set parallel to it. The atoms are excited from the ground state with two laser beams of the same wavelength counter propagating in the center between the two wires. The experimental set up provides Doppler-free spectra and allows to do Stark splitting measurements either by an optogalvanic signal from the cold wire after ionization by a third laser photon or by detecting the fluorescence photons emitted by the excited atoms. For the latter purpose a window is installed in the side-wall of the hydrogen cell and fluorescence photons are detected, after spectral and spatial filtering, by a photo multiplier optimized for pulsed operation.

Electric fields of 200 V/cm or more can be measured by excitation of the $n = 2$ level with two 243 nm laser photons. The measured spectra of both hydrogen and deuterium atoms have been shown to provide reliable results for electric field measurements. The deuterium spectra have the simpler structure due to the unresolved small hyperfine splitting and allow for more straightforward data processing. For 243 nm excitation, only optogalvanic detection is simply applicable, because the Lyman alpha fluorescence radiation is emitted in the vacuum ultraviolet spectral region. On the other hand, controlled tunable pulsed laser radiation is easier to attain at 243 nm than at 205 nm. Hence, this measurement method is preferable in cases where optogalvanic detection is possible and electric fields are high enough.

Better electric field sensitivity is obtained by observing the Stark splitting of the $n = 3$ level of atomic hydrogen. For this task the pulsed laser system has to be tunable in the deep ultraviolet region around 205 nm with a relative spectral resolution of $5 \cdot 10^6$. Excitation of the $n = 3$ level is followed by emission of Balmer alpha fluorescence radiation in the visible at 656 nm, which can be measured simultaneously with the optogalvanic detection. Both spectra give good results in comparison with calculated values based on the $n = 3$ level Stark splitting. Therefore, the detection method can be chosen according to the characteristics of the gas discharge of interest. In general, fluorescence detection has the distinction of improved spatial resolution and is not affected by the enhanced ionization in higher electric fields which introduces additional noise in any optogalvanic signal.

The sensitivity of electric field measurements is decreased and finally limited by spectral line broadening. Power broadening and the life-time reduction due to photo ionization are only negligible for irradiances not exceeding 50 MW/cm^2. Stark broadening by plasma electrons and ions is below the spectral resolution of our laser systems for electron densities of less than $2 \cdot 10^{18}$ m^{-3}.

Analysis of the measured Stark spectra revealed the frequency separation of two Stark components as the parameter most suitable for electric field determination in all cases investigated here. For linear polarization of the two laser beams perpendicular to the external field (s-polarization) and also for circularly polarized radiation exciting $\Delta m = 0$ transitions by 1s-3s/d, as well as in the case of 1s-2s excitation in general, this parameter is the frequency separation between the line components corresponding to the two-photon transitions to the upper states evolving from the field-free Lamb shifted $3S_{1/2}$ state and from the $3P_{1/2}$ state, respectively. The latter transition is forbidden in the field-free case, but due to the level mixing in an electric field the forbidden $3P_{1/2}$ component appears with increasing intensity and shifts away from the $3S_{1/2}$ component with increasing electric field strength. This frequency shift has been proven as reliable parameter for electric field determination in the cases mentioned above.

In the case of linear polarization of the two laser beams parallel to the electric field (p-polarization), the $3P_{1/2}$ component remains very weak and is practically undetectable in the measured spectra for field strengths below 500 V/cm. In this case, however, only one of the $3D_{5/2}$ and one of the $3D_{3/2}$ Stark components have significant excitation probability, in contrast to the other cases of laser polarization. The frequency separation between these two individual Stark components increases with the electric field strength and can be used as a measuring parameter for the electric field in the case of p-polarization. The transitions are allowed also at zero field, but due to the decreasing slope of their frequency shift, the low field detection limit for these two components was also found at field strengths of about 50 V/cm. This value thus represents the practical lower limit for all three cases of laser polarization investigated here. Comparison of the different cases shows that preference should be given to the circular polarization exciting $\Delta m = 0$ transitions, because the measured Stark spectrum does not depend on the direction of the electric field. In addition, the selection rules yield more pronounced $3S_{1/2}$ and $3P_{1/2}$ components in the spectrum, which facilitates the electric field determination.

As compared to other methods that require comparison of a whole measured spectrum with a set of theoretically calculated spectra, our approach is simpler without a loss of sensitivity. The advantage results from the fact that the determination of the frequency difference does not require critical line intensity information such as varying fluorescence yields or collisional mixing effects for different Stark components.

The results of the investigations performed in this work show that the one-step laser excitation method is a very convenient tool for use in the electric field diagnostics of plasma sources containing hydrogen. The laser pulse energies made available by both solid state laser systems open the possibility for sheet diagnostics as well, and the narrow laser bandwidths allow to perform electric field measurements with about 10 V/cm uncertainty, nanosecond time resolution, and a spatial resolution limited by the fluorescence detection system.

Bibliography

[1] A. Bustillo Iglesias. PhD thesis, Universidad Valladolid, 2000.

[2] U. Czarnetzki, D. Luggenhölscher, and H.F. Döbele. *Plasma Sources Sci. Technol.*, 8:230, 1999.

[3] U. Czarnetzki, D. Luggenhölscher, and H.F. Döbele. *Appl. Phys. A*, 72: 509, 2001.

[4] S.V. Ratynskaia, V.I. Demidov, and K. Rypdal. *Phys. Plasmas*, 9:4135, 2002.

[5] R.W. Warren. *Rev. Sci. Instr.*, 26:765, 1955.

[6] J. Stark. *Ann. d. Phys.*, 43:965, 1914.

[7] C. Barbeau and J. Jolly. *Appl. Phys. Lett.*, 58:237, 1991.

[8] Z. Donkó, K. Rózsa, R.C. Tobin, and K.A. Peard. *Phys. Rev. E*, 49: 3283, 1994.

[9] I.R. Videnović, N. Konjević, and M.M. Kuraica. *Spectrochim. Acta B*, 51:1707, 1996.

[10] J.E. Lawler and D.A. Doughty. *Adv. At. Mol. Opt. Phys*, 34:171, 1994.

[11] E. Schrödinger. *Abhandlungen zur Wellenmechanik 2. Aufl.* Leipzig, 1928.

[12] U. Czarnetzki, D. Luggenhölscher, and H.F. Döbele. *Phys. Rev. Lett.*, 81:4592, 1998.

[13] J.P. Booth, M. Fadlallah, J. Derouard, and N. Sadeghi. *Appl. Phys. Lett.*, 65:819, 1994.

[14] J.P. Booth, J. Derouard, M. Fadlallah, L. Cabaret, and J. Pinard. *Opt. Comm.*, 132:363, 1996.

[15] P.J. Mohr and B.N. Taylor. *Rev. Mod. Phys.*, 77:1, 2005.

[16] W. Pauli. *Z. Phys.*, 36:336, 1926.

[17] H.A. Bethe and E.E. Salpeter. *Quantum Mechanics of One- and Two-Electron Atoms.* Plenum Publishing Corp., New York.

[18] W.E. Lamb and R.C. Retherford. *Phys. Rev.*, 72:241, 1947.

[19] W.E. Lamb and R.C. Retherford. *Phys. Rev.*, 79:549, 1950.

[20] W.E. Lamb and R.C. Retherford. *Phys. Rev.*, 81:222, 1951.

[21] H.A. Bethe and L.M. Brown. *Phys. Rev.*, 77:370, 1950.

[22] R. Schlapp. *Proc. Roy. Soc. London A*, 119:313, 1928.

[23] V. Rojansky. *Phys. Rev.*, 33:1, 1929.

[24] G. Lüders. *Ann. Phys.*, 6:301, 1951.

[25] J. Seidel. Spectral Line Shapes, vol. 2. page 381, Berlin, New York, 1983. W. de Gruyter.

[26] J. Seidel. *Phys. Rev. Lett.*, 57:2154, 1986.

[27] L.S. Vasilenko, V.P. Chebotayev, and A.V. Shishaev. *JETP Lett.*, 12: 113, 1970.

[28] M. Göppert-Mayer. *Ann. Physik*, 9:273, 1931.

[29] F. Biraben, B. Cagnac, and G. Grynbberg. *Phys. Rev. Lett.*, 32:643, 1974.

[30] M.D. Levenson and N. Bloembergen. *Phys. Rev. Lett.*, 32:645, 1974.

[31] T.W. Hänsch, S.A. Lee, R. Wallenstein, and C. Wieman. *Phys. Rev. Lett.*, 34:307, 1975.

[32] W. Demtröder. *Laser Spectroscopy.* Springer-Verlag, Berlin Heidelberg New York.

[33] E. Hecht. *Optics.* Addison Wesley, San Francisco.

[34] D.K. Doughty and J.E. Lawler. *Appl. Phys. Lett.*, 45:611, 1984.

[35] E.A. Den Hartog, D.K. Doughty, and J. E. Lawler. *Phys.Rev.A*, 38: 2471, 1988.

[36] B.N. Ganguly and A. Garscadden. *Appl. Phys. Lett.*, 46:540, 1984.

[37] B.N. Ganguly. *J. Appl. Phys.*, 60:571, 1986.

[38] K.E. Greenberg and G.A. Hebner. *Appl. Phys. Lett.*, 63:4036, 1993.

[39] G.A. Hebner, K.E. Greenberg, and M.E. Riley. *J. Appl. Phys.*, 76:4036, 1994.

[40] M.D.Bowden, Y.W. Choi, K. Muraoka, and M. Maeda. *Appl. Phys. Lett.*, 66:1059, 1995.

[41] B.N. Ganguly and D.A.Dolson. *Plasma. Sources Sci. Technol.*, 9:437, 2000.

[42] J.B. Kim, T. Ikutake, M.D. Bowden, K. Muraoka, and U. Czarnetzki. *Jpn. J. Appl. Phys*, 39:299, 2000.

[43] S.A. Lee, L.U.A. Andersen, J.J. Rocca, M. Marconi, and N. D. Reesor. *Appl. Phys. Lett.*, 51:409, 1987.

[44] T. Oda and K. Takiyama. 7th International Symposium on Laser-Aided Plasma Diagnostics. page 227, Fukuoka, Japan, 1995.

[45] K. Takiyama, T. Katsuta, M. Watanabe, S. Li, T. Oda, T. Ogawa, and K. Mizuno. *Rev. Sci. Instrum*, 68:1028, 1997.

[46] V.P. Gavrilenko, H.J. Kim, T. Ikutake, J.B. Kim, Y.W. Choi, M.D. Bowden, and K. Muraoka. *Phys. Rev. E*, 62:7201, 2000.

[47] V.P. Gavrilenko, H.J. Kim, T. Ikutake, J.B. Kim, M.D. Bowden, and K. Muraoka. *Phys. Rev. E*, 63:047401, 2001.

[48] Y.W. Choi, M.D. Bowden, and K. Muraoka. *Appl. Phys. Lett.*, 69:1361, 1996.

[49] E.V. Barnat and G.A. Hebner. 12th International Symposium on Laser-Aided Plasma Diagnostics. Snowbird, USA, 2005.

[50] K. Takizawa, K. Sasaki, and K. Kadota. *Jpn.J.Appl.Phys.*, 41(2), 2002.

[51] C.A. Moore, G.P. Davis, and R. A. Gottscho. *Phys. Rev. Lett.*, 52:538, 1984.

[52] Y. Yamagata, Y. Kawano, K. Muraoka, M. Maeda, and M. Akazaki. *Jpn. J. Appl. Phys.*, 30:166, 1991.

[53] J. Derouard and N. Sadeghi. *Opt. Commun.*, 57:239, 1986.

[54] H. Debontride, J. Derouard, P. Edel, R. Romestain, N.Sadeghi, and J.P. Boeuf. *Phys. Rev. A*, 40:5208, 1989.

[55] M.P. Alberta, H. Debontride, H. Derouard, and N. Sadegi. *J. Phys. III France*, 3:105, 1993.

[56] Yoshitaka Takahashi, Toshihiko Yoshino, and Kazuya Kawasaki. *Jpn. J. Appl. Phys.*, 35:2334, 1996.

[57] E.K. Cherkasova, V.P. Gavrilenko, and A.I. Zhuzhunashvili. *J.Phys. D: Appl. Phys.*, 39:477, 2006.

[58] J.A. Blackman and G.W. Series. *J. Phys. B*, 6:1090, 1973.

[59] C. Wieman and T.W. Hänsch. *Phys. Rev. Lett.*, 36:1170, 1976.

[60] L. Cabaret, C. Delsart, and C. Blondel. *Optics. Comm.*, 61:116, 1987.

[61] M.I. de la Rosa, C. Perez, K. Grützmacher, A.B. Gonzalo, and A. Steiger. *Plasma Sources Sci. Technol.*, 15:105, 2006.

[62] U. Czarnetzki, K. Miyazaki, T. Kaiwara, K. Muraoka, M. Maeda, and H.F. Döbele. *J. Opt. Soc. Am. B*, 11:2155, 1994.

[63] J. Bokor, R.R. Freeman, J.C. White, and R.H. Storz. *Phys. Rev. A*, 24: 612, 1981.

[64] R.P. Lucht, J.T. Salamon, G.B. King, D.W. Sweeney, and N.M. Laurendeau. *Opt. Lett.*, 8:365, 1983.

[65] J. Amorim, G. Baravian, M. Touzeau, and J. Jolly. *J. Appl. Phys*, 76: 1487, 1994.

[66] J.E.M. Goldsmith. *Opt. Lett.*, 11:416, 1986.

[67] U. Meier, K. Kohse-Hoinghaus, L. Schafer, and C.P. Klages. *Appl. Opt.*, 29:4993, 1990.

[68] H. Umemoto, K. Ohara, D. Morita, Y. Nozaki, A. Masuda, and H. Matsumura. *J. Appl. Phys.*, 91:1650, 2002.

[69] M.G.H. Boogaarts, S. Mazouffre, G.J. Brinkman, H.W.P. van der Heijden, P. Vankan, J.A.M. van der Mullen, D.C. Schram, and H.F. Döbele. *Rev. Sci. Instrum.*, 73:73, 2002.

[70] P. Verkerk, M. Pinard, F. Biraben, and G. Grynberg. *Opt. Comm.*, 72: 202, 1989.

[71] J.E.M. Goldsmith and L.A. Rahn. *Opt. Lett.*, 15:814, 1990.

[72] H.W.P. van der Heijden, M.G.H. Boogaarts, S. Mazouffre, J.A.M. van der Mullen, and D.C. Schram. *Phys. Rev. E*, 61:4402, 2000.

[73] K. Grützmacher, M.I. de la Rosa, J. Seidel, A. Steiger, G. Fußmann, W. Bohmeyer, and D. Voslamber. International Workshop on Diagnostics for ITER. page 307, New York, 1996. Plenum Press.

[74] K. Grützmacher, A. Steiger, Ch. Seiser, M.I. de la Rosa, and Johannsen. International school of plasma physics workshop on diagnostics for experimental fusion reactors. page 385, New York, 1998. Plenum Press.

[75] Lochte-Holtgreven, editor. *Plasma Diagnostics.* Elsevier North-Holland, Amsterdam, 1968.

[76] A. Steiger, K. Grützmacher, and M. de la Rosa. 12th International Congress Laser 95, “Laser in Research and Engineering”. page 308, Berlin, 1996.

[77] E.S. Wachman, W.S. Pelouch, and C.L. Tang. *J. Appl. Phys.*, 70:1893, 1991.

[78] P.F. Moulton. *J. Opt. Soc. Am. B*, 3:125, 1986.

[79] M. Steiger. PhD thesis, TU-Berlin, 2000.

Danksagung

The Ph.D. work presented hare has been done at the Physikalisch-Technische Bundesanstalt Institute Berlin, at the department of Detector radiometry, group for Spectroscopy of Gases and Plasmas.

At this point I would like to thank Dr. Klaus Grützmacher, who was leading this project at the beginning. He has proposed the theme for this thesis and brought me into the world of complex laser systems used in this work.

The great acknowledgement I owe to Priv.-Doz. Dr. Joachim Seidel, the leader of my group and of the whole department, for the constructive discussions during the whole time, especially for the theoretical calculations used in the work that he had performed and for finding the financial support for finishing this work.

I am very thankful to Prof. Dr. Gerd Fußmann who has accepted to be my academic supervisor, for his useful comments about the work and for the improvements of my knowledge of plasma physics.

My deepest gratitude for the success of this work goes to Dr. Andreas Steiger. He was always helpful and supportive, starting from the ideas about experiment realization, discussions of the achieved results up to the corrections of the text of this thesis.

I would also like to thank all the colleges from my group for inspiring atmosphere and understanding. Especially I would like to thank the electronic technician Ms. Marianne Fleischer for her help and support.

Lebenslauf

Name:	MinjaGemišić Adamov
23.03.1974	geboren in Bor als Tochter von Ratomir Gemišić und Dragana Gemišić geb. Radosavljević
09.1981–06.1989	Grunschule Bor
09.1989–05.1993	Gymnasium Gymnasium “Bora Stankovic” in Bor, Leistungskurse: Mathematik, Programmierung, Rechnersysteme
10.1993–10.1998	Physik Studium Studium der angewendeten Physik, Physikalische Fakultät Universität Belgrad
05.1998–10.1998	Diplomarbeit Physikalische Fakultät Universität Belgrad Thema: Spektroskopie von Glimmentladung bei Atmosphärendruck
1998–1999	wissenschaftliche Hilfskraft Fakultät für Verkehr und Telekommunikation, Universität Belgrad Assistentin für Praktikum und Übungen in Physik
02.1999–12.2001	Magisterarbeit Zentrum für Wissenschaft und Technologische Entwicklung, Universität Belgrad Thema: Einfluss von flachem Kathodenmaterial auf Intensität und Formder Lyman- und Balmer-alpha Linien von Waserstoff und Deuteriumin einer abnormalen Glimmentladung
02.2002–08.2006	Promotionsarbeit Physikalisch-Technische Bundesanstalt Berlin Arbeitsgruppe “Spektroskopie an Gasen und Plasmen” im Fachbereich “Detektorradiometrie”
seit 10.08.2002	verheiratet mit Miroslav Adamov
01.09.2003	Sohn Tadija geboren

Selbständigkeitserklärung

Hiermit erkläre ich, die vorliegende Arbeit selbständig ohne fremde Hilfe verfaßt und nur die angegebene Literatur und Hilfsmittel verwendet zu haben.

Ich habe mich anderwärts nicht um einen Doktorgrad beworben und besitze einen entsprechenden Doktorgrad nicht.

Ich erkläre die Kenntnisnahme der dem Verfahren zugrunde liegenden Promotionsordnung der Mathematisch-Naturwissenschaftlichen Fakultät I der Humboldt-Universität zu Berlin.

Berlin, den 19.5.2006
Minja Gemišić Adamov